

# REPORT DOCUMENTATION PAGE

AFRL-SR-BL-TR-02-

Public reporting burden for this collection of information is estimated to average 1 hour per response, including the time for review of data needed, and completing and reviewing this collection of information. Send comments regarding this burden estimate or any other aspect of this collection of information, including suggestions for reducing the burden, to Washington Headquarters Services, Directorate for Information Operations and Reports (4302), 1215 Jefferson Davis Highway, Suite 1204, Arlington, VA 22202-4302. Respondents should be aware that notwithstanding any other provision of law, no person shall be subject to any penalty for failing to comply with a collection of information if it does not display a currently valid OMB control number. PLEASE DO NOT RETURN YOUR FORM TO THE ABOVE ADDRESS.

maintaining the  
reducing  
22202-

2120

1. REPORT DATE (DD-MM-YYYY) January 31, 2002		2. REPORT TYPE Final Technical Report		3. DATES COVERED (From - To) Mar 1, 1998 to Feb 28, 2001	
4. TITLE AND SUBTITLE  Control of Boundary Layer Instability in Hypervelocity Flow				5a. CONTRACT NUMBER	
				5b. GRANT NUMBER F49620-98-1-0353	
				5c. PROGRAM ELEMENT NUMBER	
6. AUTHOR(S)  Hans G. Hornung				5d. PROJECT NUMBER	
				5e. TASK NUMBER	
				5f. WORK UNIT NUMBER	
7. PERFORMING ORGANIZATION NAME(S) AND ADDRESS(ES)  California Institute of Technology 1200 E. California Blvd. Pasadena, CA 91125, USA				8. PERFORMING ORGANIZATION REPORT NUMBER	
9. SPONSORING / MONITORING AGENCY NAME(S) AND ADDRESS(ES)  AFOSR/NA 110 Duncan Avenue, Room B115 Bolling AFB DC 20332-8050				10. SPONSOR/MONITOR'S ACRONYM(S)	
				11. SPONSOR/MONITOR'S REPORT NUMBER(S)	
12. DISTRIBUTION / AVAILABILITY STATEMENT  Approved for public release; distribution is unlimited					
13. SUPPLEMENTARY NOTES Rasheed, A., "Passive Hypervelocity Boundary Layer Control Using an Ultrasonically Absorptive Surface", Ph.D. Dissertation, California Institute of Technology, 2001					
14. ABSTRACT Previous theoretical work predicted that hypersonic boundary layer instability could be controlled by ultrasonically absorptive wall treatment. Experiments were performed to test this theory by constructing a model, a 5 deg. half-angle cone, with very fine porosity on one side and a solid surface on the other, and testing it in the hypervelocity shock tunnel at Caltech.  The results show that a dramatic delay of transition could be achieved in the nitrogen flow for which the porosity was designed. In carbon-dioxide flows, for which the transition Reynolds number is much higher at the high enthalpies of the experiments, the porosity on the model is too coarse and acts like roughness, actually advancing transition. The transition delay achievable with proper porosity design promises large reduction of heat loads on launch and reentry vehicles.					
15. SUBJECT TERMS Transition, control, hypervelocity, ultrasound					
16. SECURITY CLASSIFICATION OF:			17. LIMITATION OF ABSTRACT	18. NUMBER OF PAGES	19a. NAME OF RESPONSIBLE PERSON
a. REPORT Unclassified	b. ABSTRACT Unclassified	c. THIS PAGE Unclassified	UL	37	Hans G. Hornung
					19b. TELEPHONE NUMBER (include area code) (626) 395-4551

AIR FORCE OFFICE OF SCIENTIFIC RESEARCH (AFOSR)  
NOTICE OF TRANSMITTAL DTIC. THIS TECHNICAL REPORT  
HAS BEEN REVIEWED AND IS APPROVED FOR PUBLIC RELEASE  
LAW AFR 190-12. DISTRIBUTION IS UNLIMITED.

20020402 071

# **CONTROL OF BOUNDARY LAYER INSTABILITY IN HYPERVELOCITY FLOW**

Hans G. Hornung  
California Institute of Technology  
Pasadena, CA 91125

January 31, 2002

**Final Technical Report  
AFOSR Grant F49620-98-1-0353**

Approved for public release; distribution is unlimited

Prepared for  
**AIRFORCE OFFICE OF SCIENTIFIC RESEARCH**  
100 Duncan Avenue, Suite B115, Bolling AFB, DC 20332-0001

# Contents

<b>1</b>	<b>Executive Summary</b>	<b>3</b>
<b>2</b>	<b>Background</b>	<b>4</b>
2.1	Previous Experiments . . . . .	5
2.2	Theoretical basis . . . . .	7
2.3	Objective . . . . .	9
<b>3</b>	<b>Experimental Setup</b>	<b>11</b>
3.1	T5 Hypervelocity Shock Tunnel . . . . .	11
3.1.1	Description . . . . .	11
3.1.2	Data Acquisition System and Tunnel Diagnostic Data . . . . .	13
3.1.3	Calculation of Freestream Conditions in T5 . . . . .	13
3.1.4	Flow Visualization . . . . .	14
3.2	Model and Instrumentation . . . . .	15
3.2.1	Model Configuration . . . . .	15
3.2.2	Test Section Setup . . . . .	16
3.2.3	Instrumentation . . . . .	17
3.2.4	Heat Flux Measurement . . . . .	17
<b>4</b>	<b>Experimental Results</b>	<b>20</b>
4.1	Effectiveness of the Porous Surface . . . . .	20
4.1.1	Case I: Both Sides Laminar . . . . .	20
4.1.2	Case II: Both Sides Transitional . . . . .	21
4.1.3	Case III: Porous Surface Laminar, Smooth Surface Transitional . . . .	21
4.1.4	Laminar Heat Flux . . . . .	21

4.1.5	Summary Data . . . . .	25
4.1.6	Elimination of Other Causes for the Observed Effectiveness of the Porous Surface . . . . .	25
4.1.7	Effects of Surface Roughness . . . . .	28
4.2	Resonantly Enhanced Shadowgraph . . . . .	29
5	Conclusions	31
6	Achievements	31
7	Personnel	32
8	Degrees	32
9	Honors and Awards	32
10	Publications resulting from the project	32

# 1 Executive Summary

In a collaboration with Rockwell Science Center an experiment was designed to test the theoretical results of Fedorov and Malmuth of RSC, that the acoustic instability mode that is responsible for boundary layer transition at hypersonic speeds could be damped by suitable wall porosity, with the view toward devising a method for passive control of transition. Previous experiments in the T5 hypervelocity shock tunnel at Caltech together with linear stability analysis by Candler's group in Minnesota had established the acoustic instability as being responsible for the path toward transition at the conditions tested in T5.

The design of the experiment called for extremely fine porosity consisting of 0.05 mm diameter blind holes of 5 mm depth and 0.1 mm spacing, on the surface of a  $5^\circ$  half-angle cone. After a development program the fabrication was achieved by forming a stainless-steel sheet into a conical shape that fitted precisely over the existing aluminum model. Half of the sheet was porous with some 15 million laser-drilled holes, while the other half was solid. In this manner, each tunnel run yielded a comparison of transition location with and without porosity. The transition location was detected by a distribution of thermocouple heat flux gauges.

The results showed that the porosity caused a large transition delay in nitrogen flows over a range of total enthalpy from 3 to 13 MJ/kg. These were the conditions for which the experiment was designed. A resonantly enhanced shadowgraph dramatically illustrates the effect. This method of passive boundary layer control has therefore been established as a very effective device for reducing heat loads at hypervelocity flow conditions, which must be considered seriously for practical application on launch and reentry vehicles.

The model was also tested in carbon dioxide flows. In this gas, the large amount of energy that goes into vibrational excitations causes the transition Reynolds number to increase rapidly with total enthalpy, to values up to 5 times larger than in nitrogen. This makes the porosity, which was designed for nitrogen flows, too coarse, so that, as enthalpy increases, the holes begin to act like roughness elements. Thus, it is only at low enthalpies that the porosity functions as intended, and the effect is reversed, *i. e.*, transition is advanced at high enthalpies. In order to make the porosity act correctly in carbon dioxide flows, it would be necessary to make the porosity finer.

The results of the experiment have established that the theory is correct, and that a very dramatic transition delay can be achieved by suitable wall porosity. This method of passive boundary layer control can be used to achieve large reductions in heat loads in practical applications.

## 2 Background

Heat loads and forces on hypervelocity vehicles depend critically on the location of transition from laminar to turbulent flow. Though significant progress has been made toward the understanding of transition, it is still the most severe uncertainty in the aerodynamic design of such vehicles.

Two important features of hypervelocity flow set it apart from other flow regimes with respect to the transition problem. First, the dominant instability mode at sufficiently high Mach number is the second or Mack [1] mode, in which acoustic perturbations become trapped in the boundary layer, grow in amplitude and eventually cause the boundary layer to become turbulent. This is in contrast to the situation in low speed flows, where the viscous instability is usually responsible for the path to transition. Second, the relaxation processes associated with vibrational excitation and dissociation (which occur in hypervelocity flows because of aerodynamic heating) provide mechanisms for damping acoustic waves, and may therefore be expected to affect the second mode. The effects of vibrational excitation and dissociation are quite subtle however, since they also affect the mean structure and therefore the stability properties of the boundary layer.

A large part of the experimental work on the problem of stability and transition at high Mach number has been done in cold hypersonic facilities. In such facilities, the test gas is expanded from a reservoir at relatively low temperature (of order 1000 K), so that the high Mach number is produced, not so much by raising the speed, but mainly by lowering the speed of sound. Important examples of the work in this regime are the experiments of Demetriades [2], Stetson *et al.* [3] and Kendall [4]. (Reshotko [5] presented a very good review). Together with the linear stability analysis by Mack [1], experiments of this kind provide a substantial basis for understanding the path to transition in cold hypersonic flow. They are, however, not able to capture the phenomena that occur in hypervelocity flows because of the vibrational excitation and dissociation that characterize them.

Some of the specific problems of hypervelocity boundary layer stability have been addressed computationally by a number of authors. They include the work of Malik and Anderson [6], who considered equilibrium vibration and dissociation, and Stuckert and Reed [7] who assumed vibrational equilibrium but finite-rate chemistry. Both found that the new effects caused the boundary layer to be destabilized. However, more recent work by Johnson *et al.* [8] found that non-equilibrium chemistry had a strong damping effect, in agreement with recent experimental evidence. The apparent contradiction between the results of these investigations is not too surprising, in view of the complicated manner in which the rate processes can influence the stability problem, and the many parameters involved in it.

## 2.1 Previous Experiments

Much of the work on transition in hypersonic flow has been performed on the simplest possible shape, namely the slender cone. The flow over a slender cone has the advantages that the streamwise pressure gradient is zero, and that it is free of side effects. The first experiments to be performed in the newly completed T5 hypervelocity free-piston shock tunnel in 1991-1993 were designed for a 5 deg half-angle cone also, in order to be able to compare the new high enthalpy results with those from the cold hypersonic wind tunnels. A diagram of the model built for these experiments is shown in Figure 1.

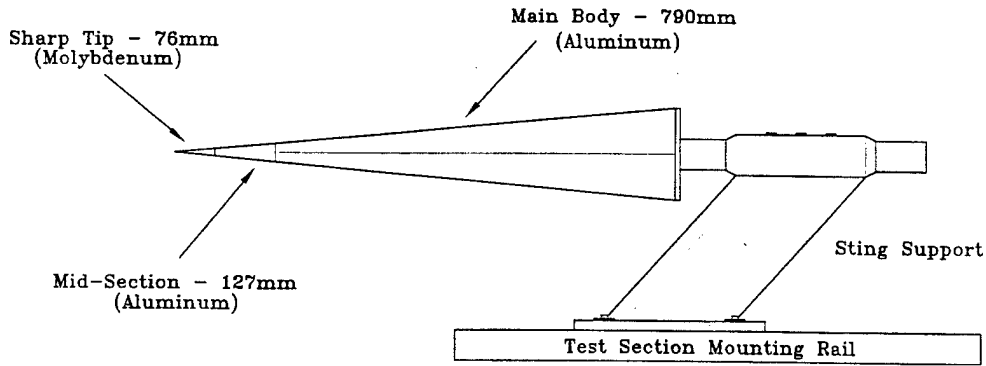


Figure 1: Slender cone model built for T5 experiments. The main body is hollow and instrumented with thermocouple surface heat flux gauges.

The first series of experiments (for details see Germain and Hornung [9]) explored the behavior of the transition location on the cone as a function of the total enthalpy of the flow in air and nitrogen. The transition location was determined from the distinct rise in heat flux. An example of how this is done is shown in Figure 2. In hypervelocity flow simulation it is important to reproduce the actual speed of the flow, so that the vibrational excitation and dissociation are reproduced correctly. This is often done at the expense of reproducing the Mach number. That is the case in the T5 experiments also, where the free-stream Mach number is typically 5.5, but the speed ranges up to 6 km/s. Thus, the boundary layer edge temperature in a free-flight situation is very different than in the T5 experiments, but the temperature profile in the inner part of the boundary layer is almost the same in both cases. This is illustrated in the calculated temperature profiles for the two cases, see Figure 3.

This comparison of the temperature profiles suggests that the T5 tests may well be suitable for comparing the high temperature real-gas effects that occur in free flight with those that occur in the T5 experiments, but it is more meaningful to compare the two in terms of the Reynolds number evaluated at the reference condition. The reference temperature is given by

$$\frac{T^*}{T_e} = 0.5 + \frac{\gamma - 1}{2} \frac{\sqrt{Pr}}{6} M_e^2 + 0.5 \frac{T_w}{T_e},$$

where the subscript  $e$  refers to the boundary layer edge conditions.

The results of experiments in nitrogen and air flows are plotted in Figure 4 in the form

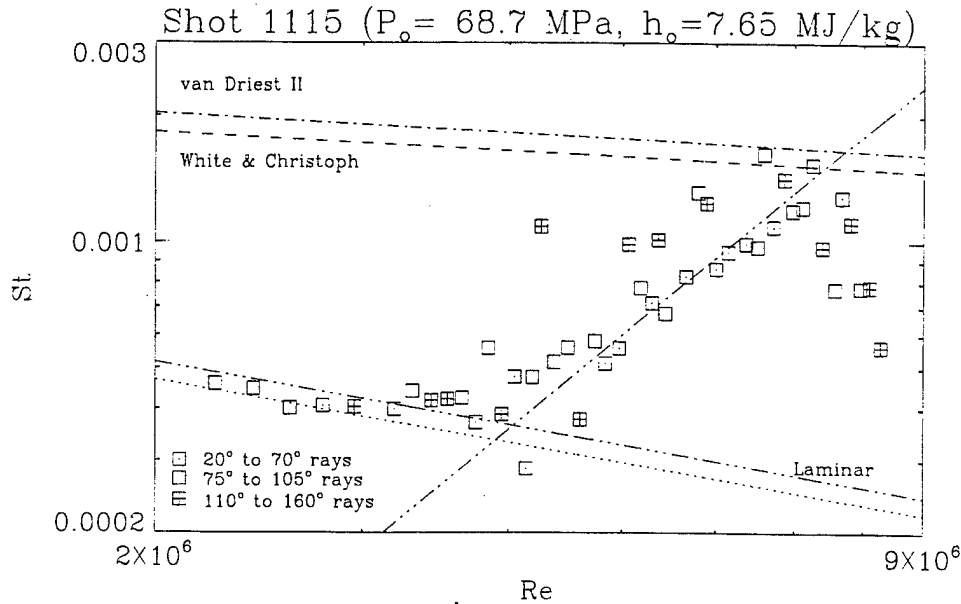


Figure 2: Plot of Stanton number against boundary-layer edge Reynolds number for one experiment on the cone. As may be seen, the Stanton number follows the theoretical laminar flow line (dotted line) at low Reynolds numbers, and rises up toward the turbulent level (as given by two turbulence models) at high Reynolds number. The transition Reynolds number is determined by a straight line fit of the transitional data.

of the Reynolds number at transition, evaluated at the reference temperature and based on the distance from the cone tip to the transition location, versus the total enthalpy of the flow. Two new features are brought out by this plot. First, a significant increase in transition Reynolds number (evaluated at reference conditions) with total enthalpy increase is observed, and second, this increase is slightly larger in air than in nitrogen. This led us to suspect that transition is significantly influenced by high-enthalpy real-gas effects, and that it might be interesting to explore what happens in other gases, such as helium, which behaves like a perfect gas in our total enthalpy range, and carbon dioxide, which exhibits strong vibrational and dissociational effects in this range. The first experiment, with helium showed that, even at 15 MJ/kg, the transition Reynolds number was the same as the low enthalpy value. A dramatically larger transition Reynolds number was observed in carbon dioxide flows, also shown in Figure 4, (for details see Adam and Hornung [10]).

It is clear from these results that a dramatic transition delay which is completely absent at low speeds is evident at high enthalpy, and that the magnitude of the phenomenon and the enthalpy at which it sets in are different for different gases.



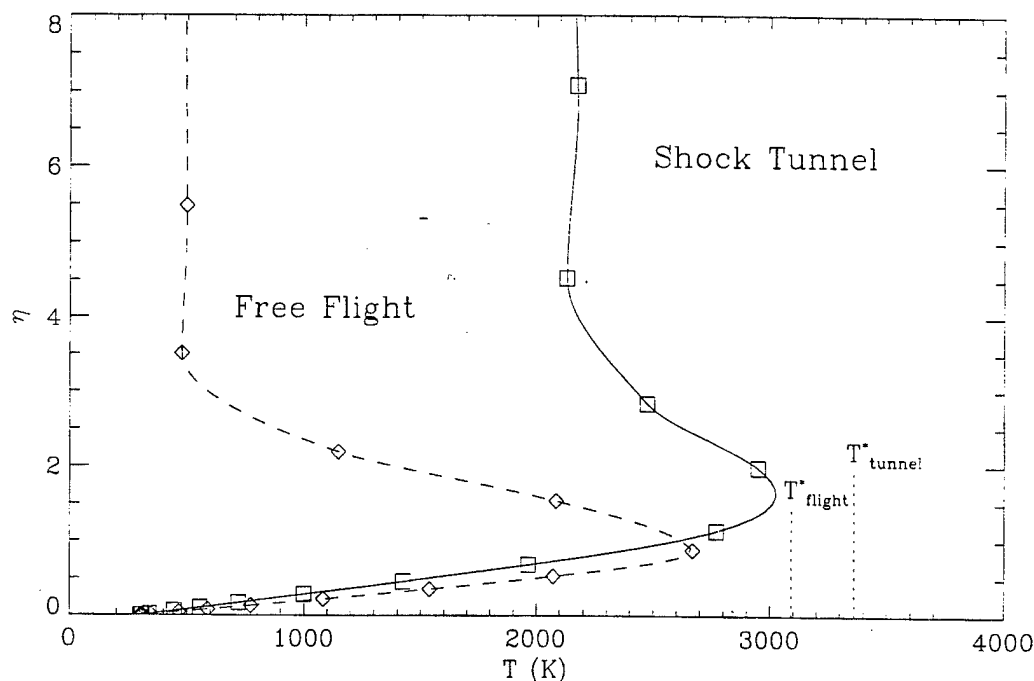


Figure 3: Typical  $T_5$  and free-flight temperature profiles in laminar boundary layer coordinates for a total enthalpy of 14 MJ/kg.

## 2.2 Theoretical basis

It was at this point that Graham Candler and his group became interested in testing our results by making linear stability computations at the conditions of our experiments. Their results agreed with the trends observed in the nitrogen and air flows, and illustrated dramatically how strongly thermochemical non-equilibrium effects can influence the growth rate of disturbances. Examples of their results are shown in Figure 5. The importance of these results for boundary layer control is that they establish the acoustic Mack mode as being responsible for the path to transition in the  $T_5$  experiments.

Just as the experiments described in the previous section had been completed, Norman Malmuth of Rockwell Science Center and Sasha Fedorov of Moscow Institute of Physics and Technology started to discuss with us the possibility of controlling transition in hypersonic flow. They had shown theoretically that the acoustic mode could also be damped by wall porosity, see Fedorov and Malmuth [11]. In the remainder of this section an outline of their results is presented.

Simply stated, the acoustic disturbances are trapped and amplified in the boundary layer, which acts like a wave guide for them. It has been known (early work on the subject included that of Kirchhoff and Rayleigh) that acoustic disturbances are absorbed in wall porosity by viscous action and heat conduction. Fedorov and Malmuth's contribution was

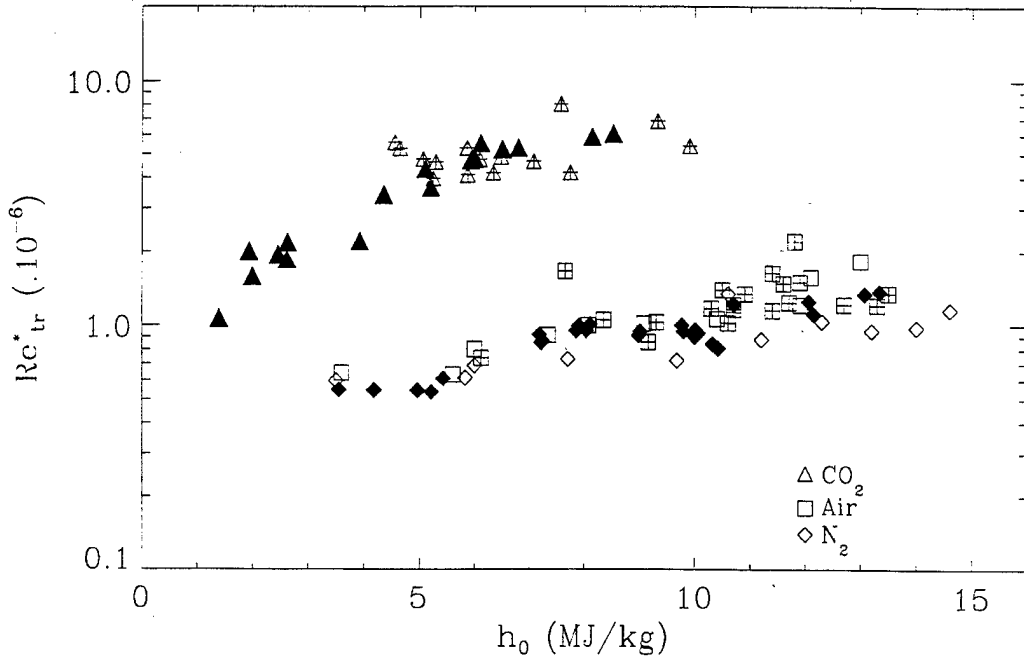


Figure 4: Transition Reynolds number observed in previous cone experiments. Open symbols are from Germain and Hornung, symbols with '+' are from Adam and Hornung, and solid symbols were added by Rasheed as part of the project of this report.

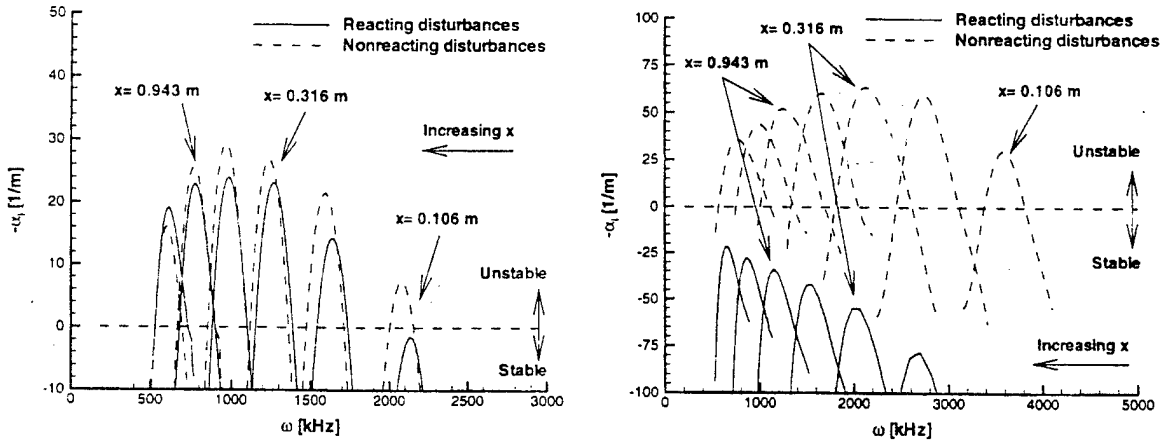


Figure 5: Results of linear stability calculations with thermochemical non-equilibrium at the conditions of T5 shot 1162 in air at 9.3 MJ/kg (left) and shot 1150 at 4.0 MJ/kg in carbon dioxide (right). The graphs show growth rate of disturbances as functions of disturbance frequency at several distances along the cone. To examine the damping effect of finite rate processes, the dotted curves show the same results but with the rate processes turned off. Note how the rate processes completely stabilize the disturbances in the case of carbon dioxide. (reproduced from Johnson *et al.* [8]).

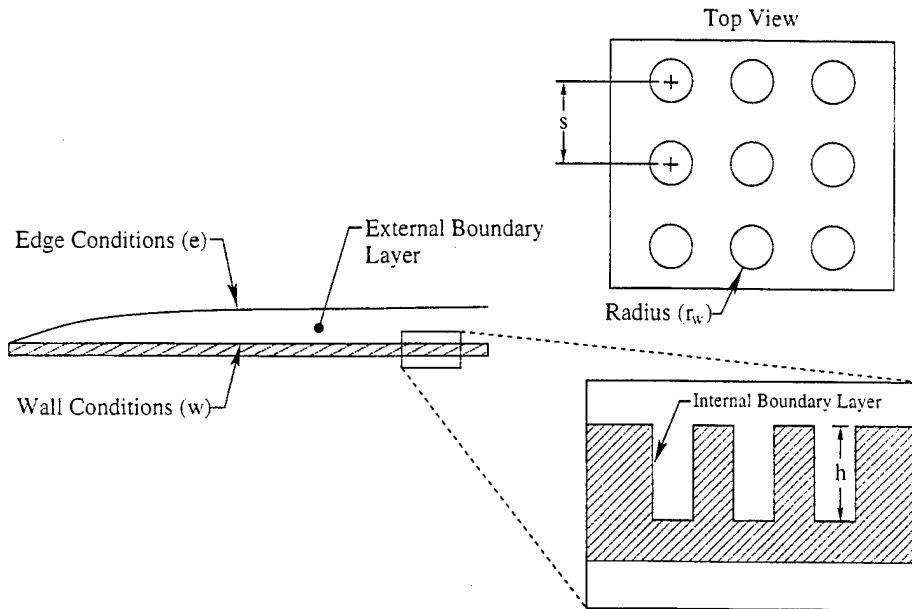


Figure 6: Schematic diagram showing the porous microstructure under consideration. The holes of radius  $r_w$  and depth  $h$  are arranged in a rectangular grid with a uniform spacing of  $s$ . The 'external boundary layer' refers to the overall boundary layer on the surface, while the 'internal boundary layer' refers to the boundary layer within a hole.

a detailed linear stability analysis of the effect of the damping afforded by this mechanism with particular kinds of wall porosity. One such scheme is shown schematically in Figure 6

An example of the results of the analysis is presented in Figures 7 and 8. The first shows, for a particular set of parameters, the growth rate of acoustic disturbances depending on the dimensionless hole diameter of porosities with a regular array of blind holes. A significant reduction is achieved by changing the hole diameter. In the second figure the dependence of the maximum growth rate on the volume ratio

$$n = \frac{\pi r_w^2}{s^2}$$

and on the dimensionless depth are shown. The latter illustrates that for a particular dimensionless hole depth, optimum damping occurs.

Our discussions with Fedorov and Malmuth then led to a collaborative effort to define a set of experiments in T5 and to write a proposal to the AFOSR to perform these experiments. The resulting project is the subject of the remainder of this report.

## 2.3 Objective

The previous set of experiments and linear stability analysis provided the basis for the current experimental study. In particular, the large database of results from the experiments

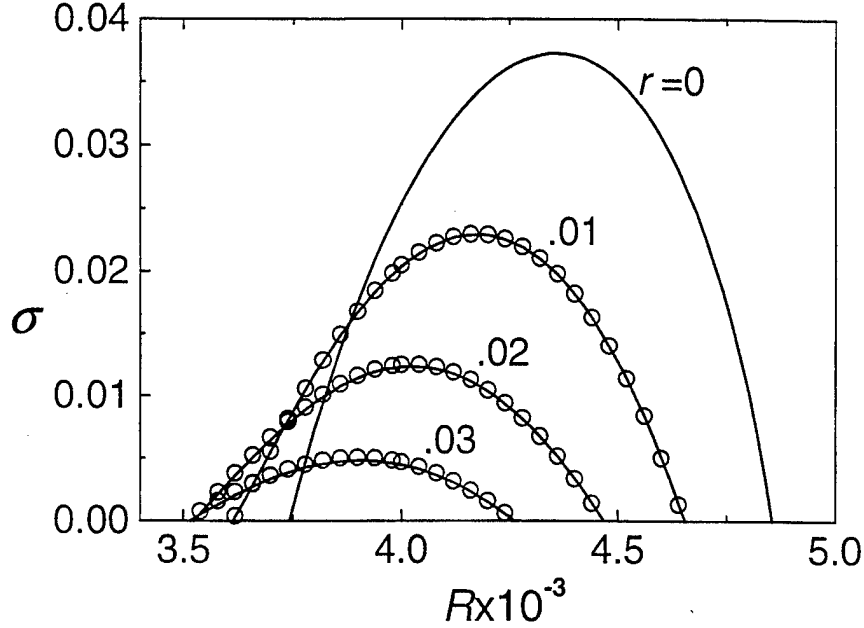


Figure 7: Plot of spatial growth rate of the second mode ( $\sigma$ ) versus Reynolds number ( $R = Re_{\delta^*} = \delta^* U_e \rho_e / \mu_e$ ) with non-dimensional radius ( $r$ ) as a parameter. The solid lines correspond to calculations using both the pressure and thermal admittance boundary conditions and the circles correspond to calculations with the thermal admittance taken to be zero. The case  $r = 0$  corresponds to a solid wall (both pressure and thermal admittance are zero). Increasing the radius of the holes (and therefore the absorption coefficient) is seen to have a strong damping effect on the growth rate;  $F^* = 2.8 \times 10^{-4}$ ,  $n = 0.5$ ,  $M=6$ ,  $Pr=0.71$ ,  $\gamma=1.4$ ,  $T_w^*/T_{ad}^*=0.2$  and  $h^* \rightarrow \infty$ . (Reproduced from Fedorov *et al.* [12])

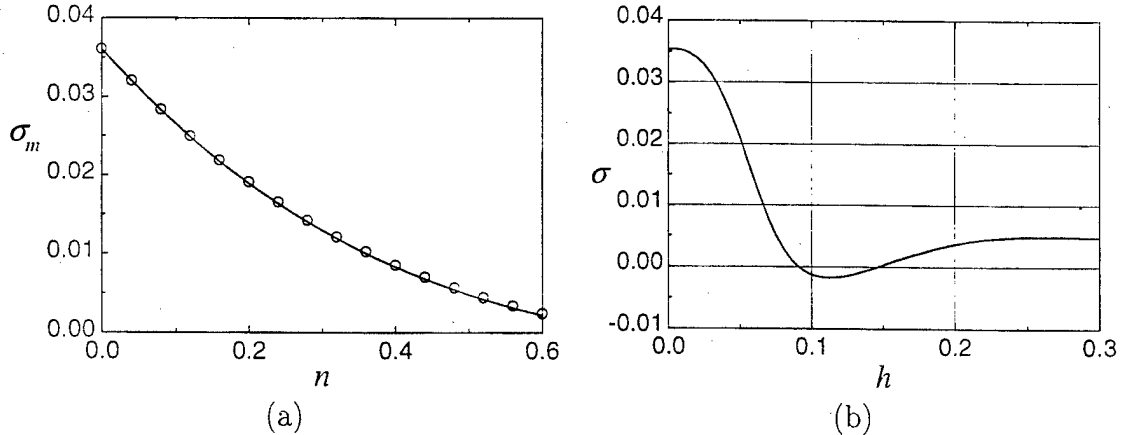


Figure 8: (a) Plot of the maximum spatial growth rate ( $\sigma_m$ ) of the second mode versus the porosity ( $n$ );  $F^* = 2.8 \times 10^{-4}$ ,  $M=6$ ,  $Pr=0.71$ ,  $\gamma=1.4$ ,  $T_w^*/T_{ad}^*=0.2$ ,  $r^*=0.03$ , and  $Re_{\delta^*} = 4000$ . Increasing the porosity is seen to increase the stabilizing effect. (b) Plot of spatial growth rate ( $\sigma$ ) of the second mode versus the non-dimensional depth of the microholes ( $h = h^*$ ); all parameters are the same as above, except  $n$  is fixed at 0.4. The damping is seen to be an optimum at  $h^* = 0.12$  and rapidly approaches a limiting value for  $h^* \geq 0.3$ . (Reproduced from Fedorov *et al.* [12])

by Germain [9] and Adam [10] provided important comparison data to serve as a checkpoint for the new results. Furthermore, the linear stability calculations by Johnson *et al.* [8] indicated that the Mack mode was indeed the dominant instability mode. Finally, Fedorov and Malmuth's linear instability calculations [12] proposed a mechanism to delay the boundary layer transition which directly addressed this mode.

The broad objective was to test the effectiveness of the proposed passive hypervelocity boundary layer control scheme. This was to be accomplished by testing a nominal  $5^\circ$  half-angle cone with a smooth surface on one side and the ultrasonically absorbing porous surface on the other side at zero angle-of-attack in the T5 Hypervelocity Shock Tunnel. As was done in the previous experiments, the transition location was determined by the use of flush-mounted heat transfer gauges. Simultaneous comparison of the results on both surfaces allowed each experiment to be self-contained with transition Reynolds number on the smooth surface providing a direct baseline for the porous surface results.

## 3 Experimental Setup

### 3.1 T5 Hypervelocity Shock Tunnel

#### 3.1.1 Description

The main purpose of this facility is to correctly simulate hypervelocity flows by matching the enthalpy similarity criteria. It is relevant to note that, when performing ground tests of scale models of flight vehicles, it is possible to match the high Mach number either by decreasing the speed of sound of the gas (by lowering the temperature) or by increasing the flow velocity. For real flight vehicles, high Mach numbers are achieved by high flight velocities. In wind tunnel testing, however, it is much easier to decrease the temperature of the test gas. This results in 'cold' hypersonic flows which duplicate some of the relevant physical flow phenomena, but not the proper chemical phenomena, such as molecular dissociation and recombination. It is apparent that the effects of chemistry can only be observed in test flows that match the high flight velocities and consequently the high temperatures. These flows are called 'hot' hypersonic flows or hypervelocity flows and can be produced in high enthalpy facilities such as the T5 Hypervelocity Shock Tunnel. Hornung [13] discusses in detail the relevant similarity criteria for hypervelocity flows and the importance of high enthalpy facilities.

This reflected shock tunnel facility consists of the six major components shown in Figure 9: the piston, the secondary reservoir (2R), the compression tube (CT), the shock tube (ST), the nozzle and the dump tank (DT). Prior to the shot, the various parts of the facility are filled with the appropriate gases depending on the run condition. The dump tank and nozzle sections are typically evacuated, while the secondary reservoir is filled with high pressure air ( $P_{2R} \simeq 2$  MPa to 10 MPa), the compression tube is filled with a helium-argon mixture

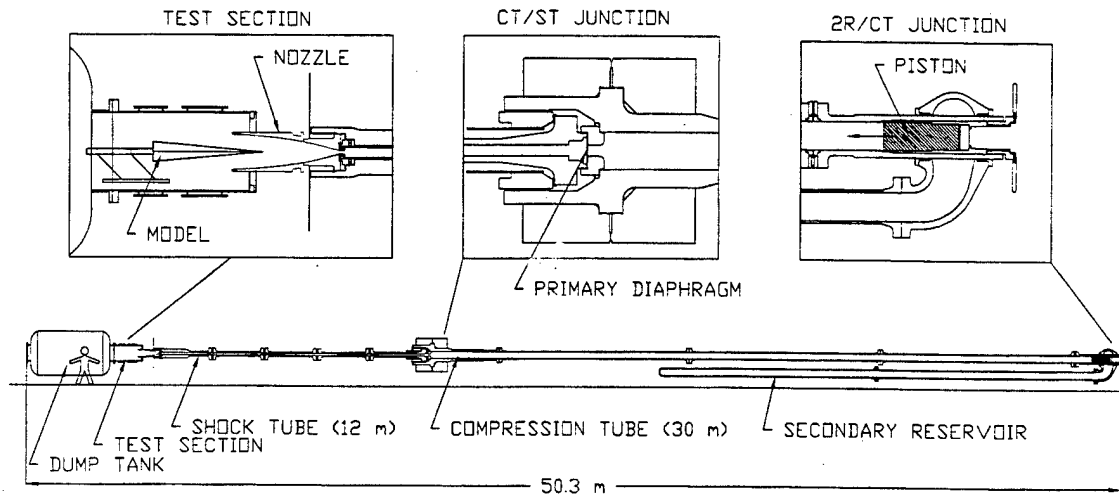


Figure 9: Schematic diagram of the T5 Hypervelocity Shock Tunnel. The six major components are the piston, the secondary reservoir, the compression tube, the shock tube, the test section and the dump tank. The outline of a person in front of the dump tank gives a sense of the overall size of the facility.

( $P_{CT} \simeq 100$  kPa), and the shock tube is filled with the desired test gas ( $P_{ST} \simeq 100$  kPa or less). It is critical to tune the various pressures to carefully control the piston motion to avoid damage to the facility.

Initially a piston is loaded at the 2R-CT junction, isolating the two from each other. An experiment begins when the piston is moved slightly forward by an injection of air pressure from behind. This initial motion uncovers slots that join the secondary reservoir and the compression tube. The high pressure from the secondary reservoir then rapidly propels the piston forward in the compression tube resulting in the adiabatic compression of the helium-argon mixture. The rising pressure bursts the primary diaphragm causing a shock wave to travel into a shock tube whose end wall is closed except for the small throat (30 mm) of the nozzle. The reflected shock from the end wall creates a quasi-constant pressure reservoir for the subsequent steady expansion through the nozzle (area ratio = 110) and into the test section. The primary diaphragm burst pressure can be varied from  $P_4 \simeq 10$  MPa to 110 MPa and is controlled by using pre-scored diaphragms of different thicknesses. With air as the test gas, shock speeds of up to 5 km/s can be obtained to produce nominal Mach 5 flows with a specific reservoir enthalpy ranging from 3 MJ/kg to 25 MJ/kg, reservoir pressures from 5 MPa to 60 MPa and reservoir temperatures from 1000 K to 8000 K. Typical flow velocities are of the order of 4 to 5 km/s. Although the reservoir maintains a constant pressure for several milliseconds, the actual useful test time is limited to 1 to 2 ms due to driver gas contamination as indicated by studies by Sudani *et al.* [14, 15]. Other detailed descriptions regarding T5 operations

and performance can be found in Hornung and Bélanger [16], Hornung *et al.* [17], and Hornung [18].

### 3.1.2 Data Acquisition System and Tunnel Diagnostic Data

The high speed data acquisition system consisted of three CAMAC-standard crates from DSP Technology capable of sampling 60 channels at 12-bit resolution. The first crate housed a GPIB crate controller module (CC-488), the trigger generator (Model 1024), an in-house manufactured laser controller and eight digitizer channels that were on four independently controlled digitizer modules (Model 2612). These were used exclusively for tunnel diagnostic instrumentation. The other two crates housed the remaining 52 channels on 26 digitizer modules (Model 2860), 52 amplifiers (Model 1402E), the GPIB crate controllers (CC-488), the system controllers (Model 4012A/4032A) and memory modules (5200/5204). Each of these crates had a total throughput of 8 MSamples/second that was available entirely for model instrumentation. The data acquisition system was controlled using software developed in-house and run on a Sun workstation.

The tunnel diagnostic instrumentation consisted primarily of PCB piezoelectric pressure transducers located along the length of the facility. Two redundant transducers ( $P_{o, \text{North}}$  and  $P_{o, \text{South}}$ ) were located diametrically opposite each other on the shock tube at a distance of 48 mm from the shock tube end wall to measure the stagnation pressure in the reflected shock region. These transducers generated the trigger signal and thus  $t = 0$  corresponds to the pressure rise in the stagnation region. Two more transducers ( $ST_3$  and  $ST_4$ ) were located at 2.37 m and 4.77 m from the shock tube end wall and were used to calculate the shock speed ( $u_s$ ). Another two redundant transducers ( $P_{4, \text{North}}$  and  $P_{4, \text{South}}$ ) were located in the compression tube just upstream of the primary diaphragm in order to measure the diaphragm burst pressure. Additional diagnostic instrumentation consisted of two linear voltage displacement transducers (LVDT) to measure the tunnel recoil. Although its signal was not recorded, an accelerometer placed near the launch end of the facility was used to generate an early trigger signal (approximately 200 ms before the stagnation pressure rise) necessary for the laser used for flow visualization.

### 3.1.3 Calculation of Freestream Conditions in T5

The flow conditions in the freestream were computed based on the nozzle reservoir conditions ( $P_o, T_o$ ) using a one-dimensional, inviscid, vibrational equilibrium, chemical non-equilibrium nozzle code (NENZF) written by Lordi *et al.* [19]. The output consisted of all relevant flow parameters including pressure ( $P_\infty$ ), temperature ( $T_\infty$ ), density ( $\rho_\infty$ ), velocity ( $u_\infty$ ), Mach number ( $M_\infty$ ), and chemical species concentrations. Although not used, a two-dimensional code (SURF) written by Rein [20] was also available to obtain flow profiles at the nozzle exit. This code was, in fact, used during T5 nozzle calibration studies by Rousset [21].

The nozzle reservoir pressure ( $P_o$ ) was measured directly as the average of the two redundant transducers ( $P_{o, \text{North}}$  and  $P_{o, \text{South}}$ ) and was used as one of the inputs for the NENZF code. The other reservoir conditions, such as temperature ( $T_o$ ) and enthalpy ( $h_o$ ), were computed based on the initial shock tube conditions ( $P_{ST}, T_{ST}$ ) and the measured incident shock speed ( $u_s$ ).

This calculation was a one-dimensional equilibrium gasdynamics reflected-shock problem and was performed using the StanJan code written by Reynolds [22]. The thermodynamic properties used in StanJan were based on JANAF curve fits for each relevant species. Another program, the Equilibrium Shock Tube Calculation (ESTC) code by McIntosh [23], was also available and used a simple harmonic oscillator model to compute the relevant thermodynamic quantities. The calculated reflected-shock pressure was typically different from the measured pressure due to slightly off-tailored operation and two-dimensional effects. The mismatch between the two was resolved by assuming an isentropic expansion (or compression, as necessary) to the actual measured stagnation pressure. The enthalpy is referenced to 0 K with reference values of 0.0 MJ/kg for nitrogen and -8.93 MJ/kg for carbon dioxide.

### 3.1.4 Flow Visualization

The T5 test section was setup with 203 mm optical windows for flow visualization. In the past, flow visualization techniques included the use of schlieren, shadowgraphy, interferometry, and holographic interferometry. For the present series of experiments, increased sensitivity was required resulting in the use of resonantly enhanced shadowgraphy, which was initially used in T5 by Germain [9, 24] and subsequently further developed by Lemieux [25]. Further details about this technique can also be found in Bershader *et al.* [26]. In summary, this technique relies on the fact that the refractivity of a gas at its spectral line is several orders of magnitude greater than its general value at other wavelengths. This 'enhanced refractivity' can be used to greatly increase the sensitivity of any optical technique that relies on the index of refraction (*i.e.*, shadowgraphy, schlieren, and interferometry) by using a light source that is specifically tuned to be slightly off from the peak absorption wavelength. For work in T5, the flow was seeded with sodium, which has absorption lines in the visible spectrum (the sodium D-lines). The light source was a tunable dye laser (587-594 nm) built by Cummings [27], pumped by a 300 mJ/pulse frequency doubled Nd:YAG laser (532 nm) with a pulse width of 7 ns.

In practice, the issue of seeding the flow with sodium in a repeatable manner was quite difficult. In Germain's experiments, it was possible to deposit small amounts of saline solution near the expected transition point and allow the water to evaporate, leaving a thin film of salt crystals. The sodium ions resulting from the dissociation of these crystals (due to the hot flow) were sufficient to produce the required image and the crystals (approximately 100  $\mu\text{m}$  in height as measured by Germain [24]) were shown not to effect the transition location. For the present experiments, this technique was not possible because it would contaminate the porous surface. For this reason, it was necessary to limit the location of the salt deposition to the tip of the cone. It was found that Germain's technique was not as effective in such a situation since the sodium tended to disperse by the time it reached the typical transition point (roughly half-way along the length of the model). The resulting image was a standard shadowgraph which was not sensitive enough to highlight the boundary layer. This was rectified by ensuring a significant amount of salt crystals was present on the tip. This was done by dipping 10 mm of the cone tip into a super-saturated saline solution and then



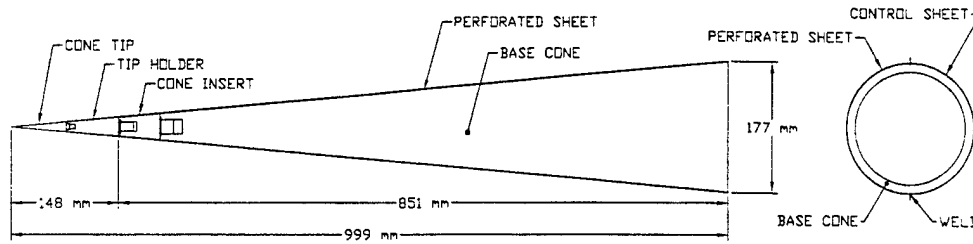


Figure 10: Schematic diagram of the assembled test model from the profile and rear view. The ‘cone sheet’ consisting of the perforated and solid sheets welded along the seams was attached to the base cone by means of a thermal interference fit.

drying it with a heat gun. The result was that the first 10 mm of the cone tip was coated in fine sodium crystals in a random distributed roughness pattern. In addition, actual raw sodium was smeared circumferentially on the cone tip holder (approximately at the 100 mm location) immediately prior to closing the tunnel for the upcoming shot. This needed to be done quickly and with care since sodium reacts violently with moisture in the surrounding air. Once again, experiments were performed to verify that the increased salt and sodium deposition did not affect the transition location results.

## 3.2 Model and Instrumentation

### 3.2.1 Model Configuration

The model used for these experiments was a heavily modified version of the same model used by Germain [9] and Adam [10]. Its design and manufacture are of particular interest due to the unique challenges involved.

The final configuration was a sharp  $5.06^\circ$  half-angle round cone consisting of five pieces with an overall length of 999 mm. It had a smooth surface over half the cone and the absorptive porous surface over the other half beginning at 148 mm from the cone tip (see Figure 10). The aluminum 6061 (Al 6061) ‘base cone’ used by Germain [9] and Adam [10] was originally constructed in two halves with a ‘dove tail’ design that allowed them to be joined together without the use of mechanical fasteners that would disturb the boundary layer. It was lengthened by the ‘cone insert’ for the purposes of this project. The base cone was already hollow to allow room for instrumentation and this aspect was preserved. An intermediate piece made of stainless steel 304L (SS 304L) referred to as the ‘cone tip holder’ was screwed into this assembly. The molybdenum cone tip screwed into this intermediate piece and was replaceable in the event of excessive blunting or other damage. Extreme care was taken during the manufacturing process to minimize the steps at these junctions.

The ‘cone sheet’ was manufactured by rolling two initially flat sheets of metal (one perforated, one smooth) to form two longitudinal halves of a cone and then laser fusion welding them along the seams. Refer to Figure 11a for a micrograph of the weld. The resulting stainless

steel cone sheet was then fitted over the aluminum base cone using a thermal interference fit that took advantage of the mismatch in thermal coefficients of expansion of the two materials. This assembly technique resulted in the cone sheet being stretched tightly over the base cone which provided the bottom for the blind microholes for the porous surface. The final porous surface had  $60 \pm 4 \mu\text{m}$  diameter holes spaced  $100 \pm 7 \mu\text{m}$  apart in a rectangular grid arrangement resulting in a porosity of 28%. The thickness of the sheet (thus the depth of the holes) was  $450 \mu\text{m}$  (26 gauge sheet). Refer to Figure 11b for a micrograph of the porous surface.

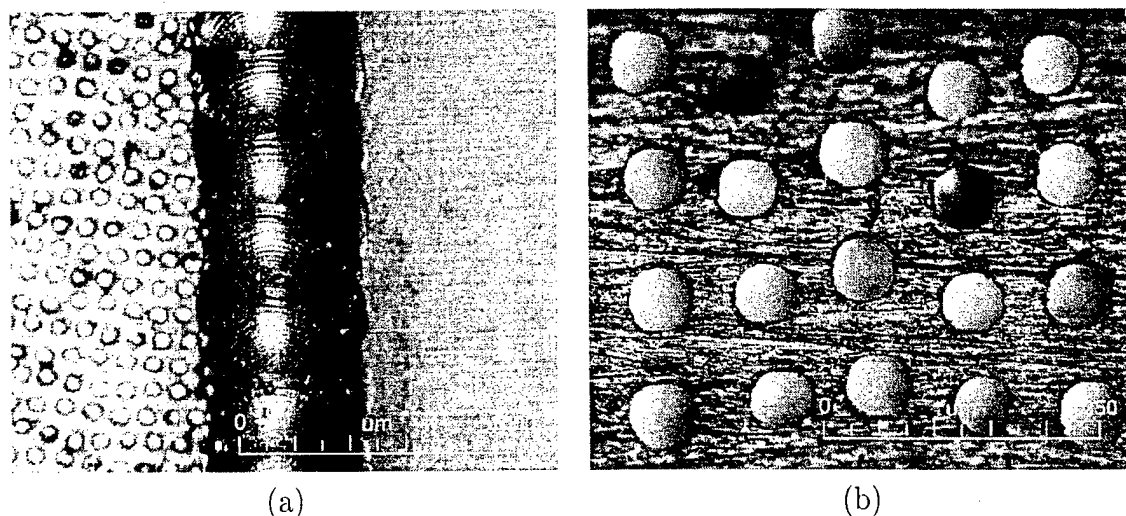


Figure 11: (a) Micrograph of the weld joining the perforated and solid sheet. The quality of the weld can be fully appreciated if one notes the scale on the micrograph. (b) Micrograph of the perforated sheet. The holes were measured to be  $60 \pm 4 \mu\text{m}$  in diameter and spaced  $100 \pm 7 \mu\text{m}$  apart (center-to-center). Note that the hole depth is twice as large as the length of the 2.5 mm scale bar.

Due to the nature of the laser drilling process, the holes were slightly conical (taper angle of about  $0.5^\circ$ ) with the small diameter exposed to the flow. Static acoustic absorption tests of this surface and other candidate materials that were considered during the design process are described in the attached thesis. It should be noted that all surfaces that were exposed to the flow were made of SS 304L, with the exception of the removable tip which was made of molybdenum.

### 3.2.2 Test Section Setup

As with Germain and Adam's experiments, the model was positioned such that the tip protruded approximately 330 mm into the nozzle during the test time. In the previous work, however, the model axis was deliberately placed approximately 64 mm above the nozzle centerline in order to maximize the length of the instrumented surface that was in the core flow (previous experiments only instrumented one longitudinal half of the model). For the present experiments, this was not acceptable since measurements were being made

around the entire circumference of the model. The axis of the cone was aligned to within 1.5 mm of the centerline of the nozzle and it was at  $0^\circ \pm 0.05^\circ$  angle-of-attack. Assuming a  $M = 5$  flow, the expansion fan from the nozzle lip was estimated to impinge on the model at approximately 800 mm from the tip (*i.e.*, near thermocouple #25). The details of the alignment procedure are described by Germain [24].

### 3.2.3 Instrumentation

The model was instrumented with 56 Type E (constantan-chromel) flush-mounted coaxial thermocouples of which 52 (26 per side) were actually used to collect data since this was the maximum number of channels available on the data acquisition system. The thermocouples were arranged in a staggered pattern typically 24.5 mm apart with the first one located 255 mm and the last one located at 814 mm from the tip. All measurements of thermocouple locations are given as measurements along the surface of the cone (and not along the axial length). Figure 12 is a schematic diagram showing the location of the thermocouples on a developed view of half the cone (*i.e.*, the smooth surface side). The porous surface side had the mirror image of the same layout. It should be noted that the thermocouples were deliberately placed as far from the weld as possible with the closest one being placed along the 40 degree ray. This is deemed more than adequate since experiments by Mee [28] in hypervelocity flow over a flat-plate (conducted in the T4 facility at the University of Queensland) indicated that the spreading half-angle of turbulent bursts is approximately 3 to 4 degrees.

The small (2.5 mm diameter) and fast response ( $1 \mu s$ ) thermocouples were manufactured in-house based on a modified design originally developed by Sanderson [29] and whose performance was tested in detail by Davis [30]. During the shot, the thermocouple signal was amplified by a factor of 500 and then sampled at 200 kHz. The sampled voltage levels were then converted to time histories of temperature rise using correlations for Type E thermocouples obtained from the National Institute of Standards and Technology [31].

### 3.2.4 Heat Flux Measurement

In general, the heat flux to a surface can be determined at discrete locations from the time resolved temperature traces measured by thermocouples. For the present experiments, since the test time was so short, the thermal penetration depth was quite small and it was sufficient to assume one-dimensional unsteady heat conduction in a semi-infinite solid with constant thermal properties. This is described by the following linear partial differential equation and boundary conditions:

$$\frac{\partial^2 T}{\partial y^2} = \frac{1}{\alpha} \frac{\partial T}{\partial t}, \quad (1)$$

$$T(y, 0) = T_i, \quad T(0, t) = T_i + \Delta T(t), \quad (2)$$

Thermocouple	Angle	Distance		Thermocouple	Angle	Distance	
		in	mm			in	mm
1	90	10.05	255.3	15	70	22.05	560.1
2	80	11.05	280.7	16	60	23.05	585.5
3	100	11.55	293.4	17	40	24.05	610.9
4	90	12.55	318.8	18	50	25.05	636.3
5	80	13.55	344.2	19	90	26.05	661.7
6	70	14.55	369.6	20	100	26.55	674.4
7	60	15.55	395.0	21	110	27.55	699.8
8	90	16.05	407.7	22	120	28.55	725.2
9	100	17.05	433.1	23	130	29.55	750.6
10	110	18.05	458.5	24	140	30.55	776.0
11	120	19.05	483.9	25	90	31.55	801.4
12	130	20.05	509.3	26	80	32.05	814.1
13	90	20.55	522.0	27	70	33.05	839.5
14	80	21.05	534.7	28	60	34.05	864.9

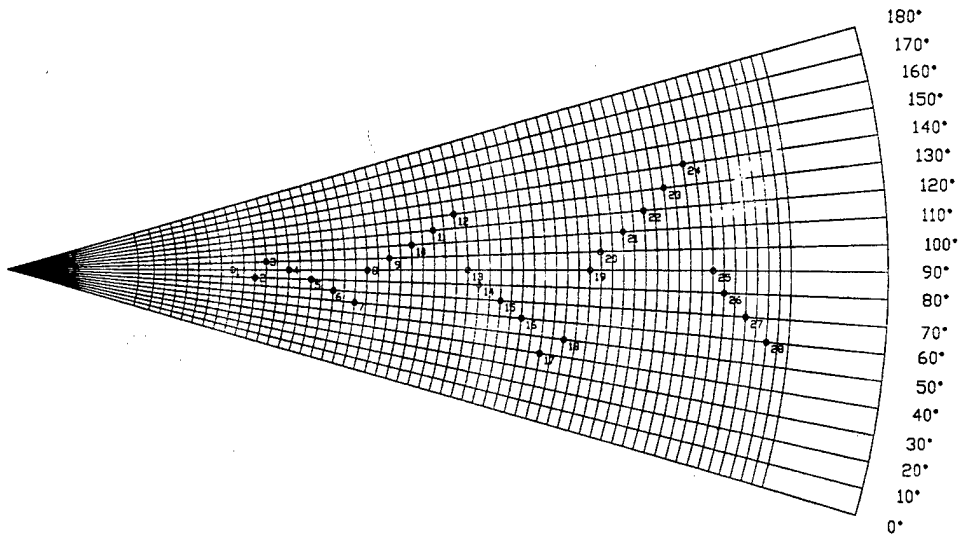


Figure 12: Schematic diagram showing the locations of the thermocouples on a developed view of half the cone (*i.e.*, the smooth side). The porous side has the mirror image of the same layout (*i.e.*, add 180° to the angular locations). The azimuthal lines are drawn at 12.7 mm (0.5 in) intervals with the second line located at 165 mm (6.5 in). The first line shows the location of the cone tip holder/cone sheet interface at 148 mm (5.8 in). All distances are measured along the surface of the cone (not along the axis).

$$\left. \frac{\partial T(t)}{\partial y} \right|_{y \rightarrow \infty} = 0, \quad \left. \frac{\partial T(t)}{\partial y} \right|_{y=0} = \dot{q}(t), \quad (3)$$

where  $T$  is the temperature,  $y$  is the distance normal to the surface,  $\alpha = k/\rho C_p$  is the thermal diffusivity ( $k$  is the thermal conductivity,  $\rho$  is the density, and  $C_p$  is the specific heat at constant pressure), and  $\dot{q}$  is the heat flux.

A number of approaches exist to solve the above problem and the relative merits of each are described in detail in Appendix B of Davis [30]. The first method, known as the ‘direct method’, developed by Schultz and Jones [32], uses Laplace transforms to directly obtain the heat flux as a function of surface temperature. Another technique, known as the ‘indirect method’, is attributed to Kendall *et al.* [33]. This involves first integrating the time-resolved surface temperature to obtain the total heat transferred to the surface (the ‘integrated heat’) and then taking the derivative of this to obtain the heat transfer rate. An inherent feature of this approach is that the integration automatically smoothes the time-resolved data, effectively acting as a filter. This latter technique was used by both Germain [9] and Adam [10] to calculate the heat flux.

For the present experiments, a spectral deconvolution method using fast Fourier transforms implemented by Sanderson [29] was used. The advantages of this technique are that it is much faster to compute and it allows more control over the signal noise filtering. The details of this technique are given in Sanderson [29] and Davis [30], and are summarized here.

Recognizing that the heat conduction equation is linear, the transient solution of this system can be described by the convolution integral

$$\Delta T(y, t) = \int_0^t g(y, t - \tau) \dot{q}(\tau) d\tau, \quad (4)$$

where the unit impulse response function,  $g(x, t)$ , is

$$g(y, t) = \sqrt{\frac{\alpha}{\pi k^2 t}} \exp \frac{-y^2}{4\alpha t}; \quad t > 0. \quad (5)$$

Fast Fourier transform techniques described in Press *et al.* [34] allow the heat flux to be determined from the measured noisy, discrete, time-resolved surface temperature data. The measured signal,  $s(t)$ , is assumed to consist of the actual temperature,  $\Delta T(t)$ , and an uncorrelated noise component,  $n(t)$ . The resulting expression for the heat transfer is

$$\dot{q}(t) = FFT^{-1} \left[ \frac{S(f) \Phi(f)}{G(f)} \right], \quad (6)$$

where capital letters are used to denote the fast Fourier transforms of the given quantities and  $\Phi(f)$  is the least-squares optimal filter given by

$$\Phi(f) = \frac{|S(f)|^2 - |N(f)|^2}{|S(f)|^2}. \quad (7)$$

As described by Davis [30], for these experiments, it is difficult to characterize the noise spectrum,  $|N(f)|^2$ , and for this reason a simple low-pass filter is used with a typical cut-off frequency of 20 kHz. This is adequate since the temperature data of interest consists almost entirely of low frequencies (less than 10 kHz) and, regardless, the 3 dB bandwidth of the amplifiers is 50 kHz.

As indicated previously, the above analysis assumed constant thermal properties, but these values have yet to be defined. For the purpose of this analysis, it has been shown by Davis that it is adequate to use values of  $\alpha$  and  $k$  that are the averages of the properties of constantan and chromel at 300 K. These average values were determined to be  $\alpha = 5.49 \times 10^{-6} \text{ m}^2/\text{s}$  and  $k = 20 \text{ W/m}^\circ\text{C}$  and were based on the thermal properties of constantan and chromel documented in Sundqvist [35]. The final quantity required, the thermocouple junction depth  $y$ , was measured by Davis [30] to be approximately  $1 \text{ }\mu\text{m}$ .

## 4 Experimental Results

### 4.1 Effectiveness of the Porous Surface

The previous experiments indicated that there is a strong relationship between reference transition Reynolds number and stagnation enthalpy. This was of particular interest since this trend was attributed to chemical damping of the Mack mode which was the mode the porous surface was seeking to control. There was further evidence to believe that the effectiveness of the porous surface would scale in a similar manner since calculations by Johnson *et al.* [8] in air indicated that the most unstable mode frequencies varied with stagnation enthalpy. For these reasons, the current tests were performed over a range of enthalpies. Before extending the results to the porous surface, however, it was necessary to validate the present results of the smooth surface with similar experiments performed by previous researchers. Three representative cases at high, mid, and low enthalpies are described below, with detailed comparisons to previous experiments by Germain [9]. This is followed by summary data plots for the nitrogen and carbon dioxide shots in order to perform general comparisons with previous results obtained by Germain [9] and Adam [10], and to elucidate any observable trends with stagnation enthalpy.

#### 4.1.1 Case I: Both Sides Laminar

Figure 13 shows plots of  $St$  versus  $Re_x$  obtained from shot 1960, a high enthalpy shot ( $h_o = 12.8 \text{ MJ/kg}$ ) in nitrogen. The plots show that the boundary layer was laminar over the entire length of the cone for both the smooth and porous surfaces. Furthermore, the results obtained on the smooth surface are shown to be in excellent agreement with previous results obtained by Germain for essentially the same run condition. Note that Germain's data indicates that the boundary layer is just beginning to transition towards the back of

the model, while this effect is not evident in the present experiment. This is attributed to the slight differences in the freestream conditions between Germain's and the present experiments.

#### 4.1.2 Case II: Both Sides Transitional

Figure 14 shows plots of  $St$  versus  $Re_x$  for shot 1963, which was a mid-enthalpy shot ( $h_o = 7.2$  MJ/kg) in nitrogen. These plots show typical transition behavior with the data following the theoretical laminar curve at low Reynolds number and moving to the expected turbulent curve further downstream. A comparison of the two plots shows that the boundary layer on the smooth surface transitions before the porous surface boundary layer. This appears to validate the prediction by Fedorov and Malmuth. Once again, Germain's data for a similar run condition is shown for comparison with excellent agreement as to the transition location.

#### 4.1.3 Case III: Porous Surface Laminar, Smooth Surface Transitional

Figure 15 shows plots of  $St$  versus  $Re_x$  obtained from shot 1976, a low-enthalpy shot ( $h_o = 5.0$  MJ/kg) in nitrogen. In this particular case, the smooth surface boundary layer transitions roughly at the half way point on the cone while the porous sheet boundary layer is laminar all the way to the end of the cone. This shot clearly demonstrates the dramatic effect of the porous surface in delaying boundary layer transition. Once again, notice the good agreement with the previous experiment performed by Germain.

#### 4.1.4 Laminar Heat Flux

Figures 13 to 15 suggest interesting trends with respect to the laminar heat flux levels. Note, for a given shot, the theoretical laminar line plotted on both the smooth and porous surface plots is the same line and can be used as a visual reference to qualitatively compare the relative magnitudes of the heat flux levels on both surfaces.

On the smooth surface, the experimentally fitted laminar line was typically close to the theoretical laminar line and, although not shown in the present figures, it tended to be above the theoretical line at higher enthalpies. This trend was also observed in the experiments by the previous researchers and was found to be more pronounced in gases which had lower dissociation energies, such as carbon dioxide. For these reasons, it is attributed to an increase in the local heat flux level due to non-equilibrium chemistry, specifically the exothermic recombination reactions that occur at the wall.

In the present experiments, the laminar heat flux level on the porous surface tended to be lower than on the smooth surface. This would be possible if the porous surface thickened the

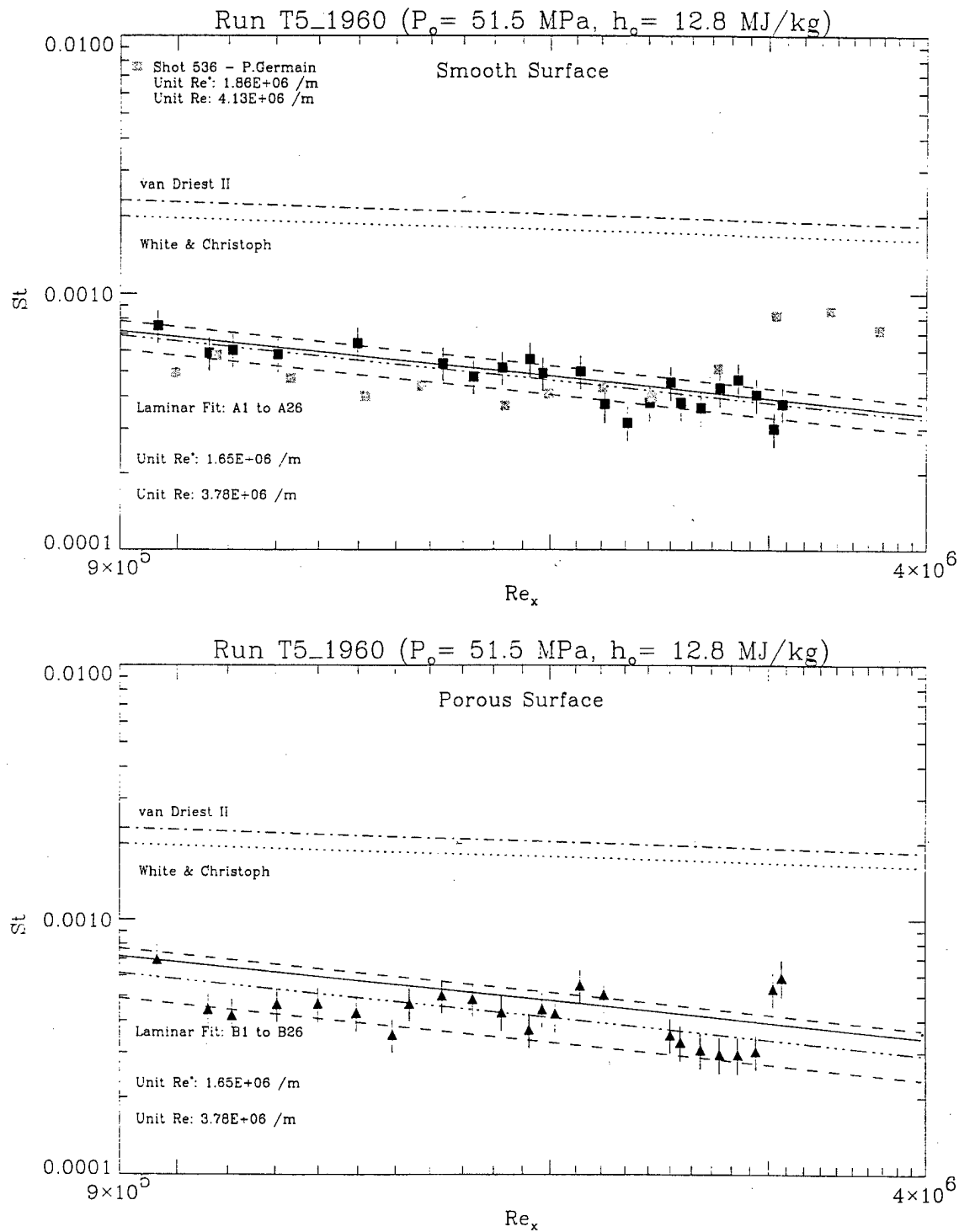


Figure 13:  $St$  versus  $Re_x$  plots obtained for shot 1960 ( $P_o = 51.5$  MPa,  $h_o = 12.8$  MJ/kg) in nitrogen test gas. The top and bottom plots show the data (obtained from the same shot) for the smooth and porous surfaces, respectively. The dark black symbols correspond to the present experiment and the grey symbols correspond to a previous experiment by Germain for essentially the same run condition. Note that both the smooth and porous surface boundary layers are laminar.



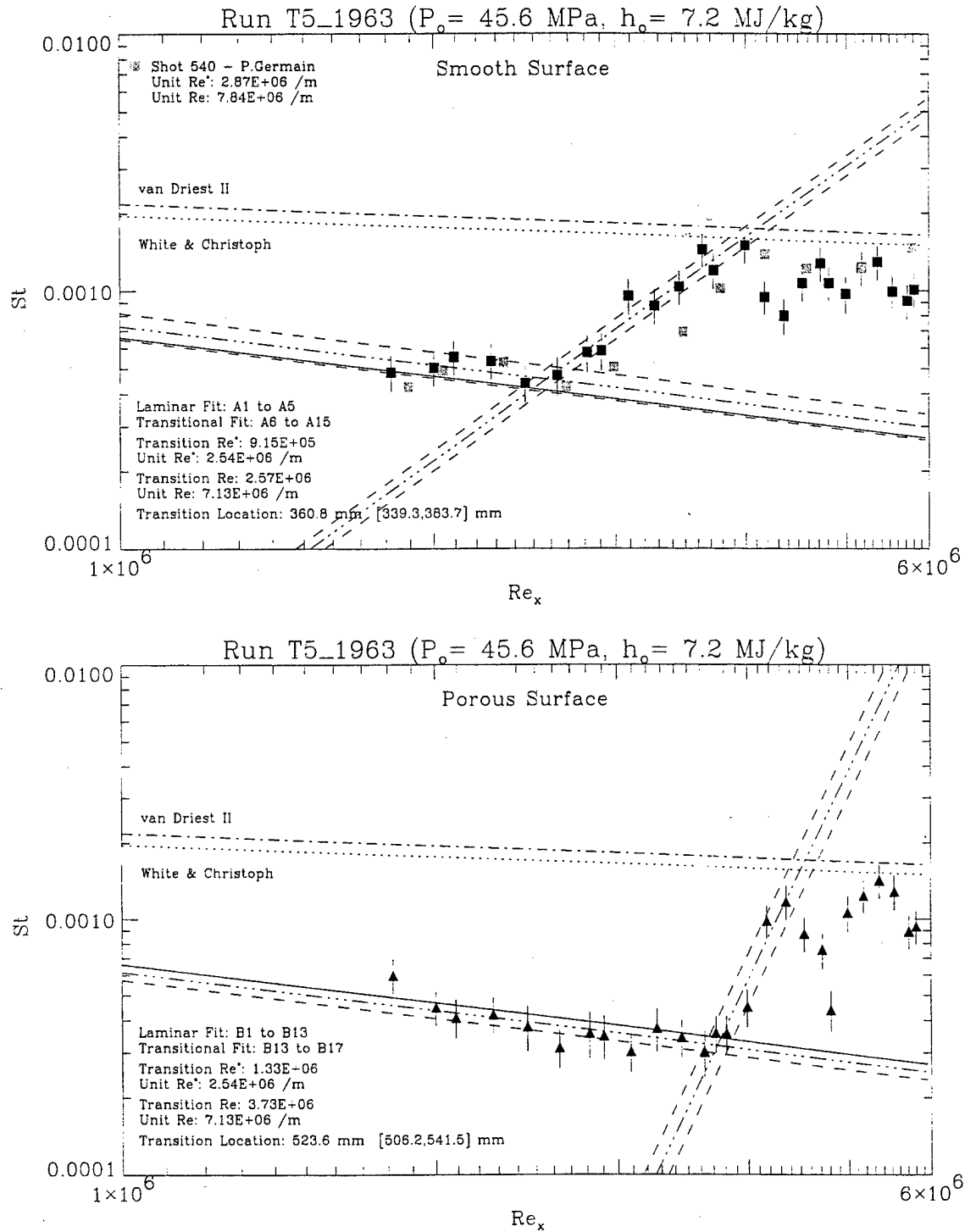


Figure 14:  $St$  versus  $Re_x$  plots obtained for shot 1963 ( $P_o = 45.6$  MPa,  $h_o = 7.2$  MJ/kg) in nitrogen test gas. The top and bottom plots show the data (obtained from the same shot) for the smooth and porous surfaces, respectively. The dark black symbols correspond to the present experiment and the grey symbols correspond to a previous experiment by Germain for essentially the same run condition. Note that both the smooth and porous surface boundary layers are transitional.

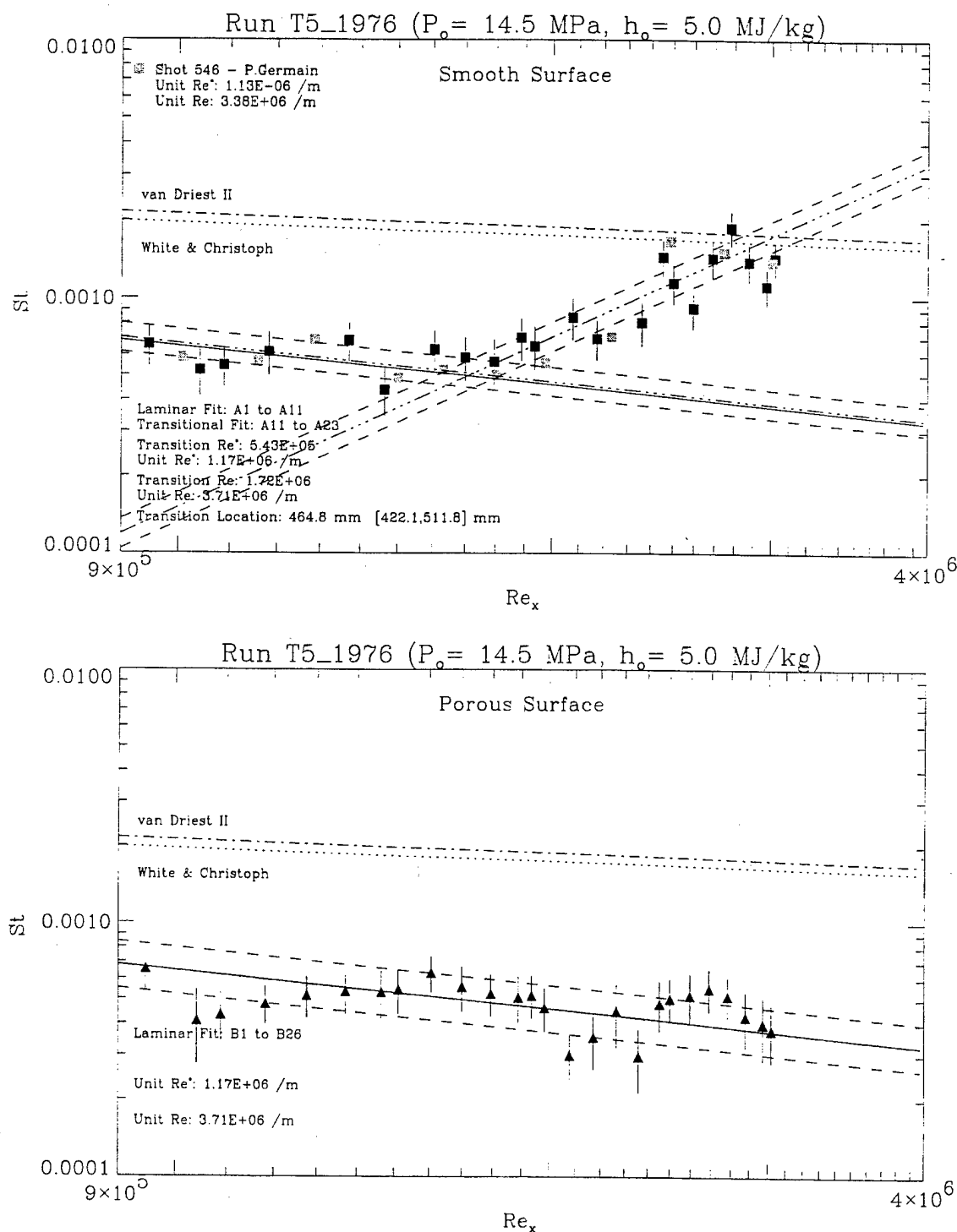


Figure 15:  $St$  versus  $Re_x$  plots obtained for shot 1976 ( $P_o = 14.5$  MPa,  $h_o = 5.0$  MJ/kg) in nitrogen test gas. The top and bottom plots show the data (obtained from the same shot) for the smooth and porous surfaces, respectively. The dark black symbols correspond to the present experiment and the grey symbols correspond to a previous experiment by Germain for essentially the same run condition. Note that the smooth surface boundary layer transitions to turbulent boundary layer, but the porous surface remains laminar.

boundary layer relative to the smooth surface. Approximate measurements of the boundary layer thickness from a shadowgraph image (see Section 4.2), however, show no measurable difference between the thicknesses on the two surfaces. Another possible explanation is that the porous surface somehow modifies the effective catalyticity of the wall and suppresses the wall recombination reactions. In addition, it was observed that the laminar heat flux level tended to be lower than the theoretical estimate. This trend is even more puzzling since the theoretical laminar line should represent the lower bound on the heat flux level. It should be added that it is difficult to say with absolute certainty that the observed differences are real since the theoretical line falls within the uncertainty bounds of the experimental fit.

#### 4.1.5 Summary Data

##### *Nitrogen Shots*

Figure 16 gives a summary of the data for the nitrogen shots. The first observation is that the present experimental results agree fairly well with the previous results obtained by Germain. The second observation is that, in all cases, the porous surface delayed transition by a significant amount. The open diamonds with an upwards facing arrow ( $\uparrow$ ) indicate that the porous surface boundary layer was laminar to the very end of the cone. The value plotted assumes that transition occurred at the last thermocouple (*i.e.*, unit Reynolds number multiplied by the last thermocouple location). This is not a valid data point, but rather a manner in which to show that the boundary layer was entirely laminar. The same discussion applies for the open square symbols with a ( $\uparrow$ ) for the smooth surface side. The two data points at 13 MJ/kg are actually open diamonds superimposed on open squares with an  $\uparrow$ , indicating that both the smooth and porous surface boundary layers were entirely laminar. It is interesting to note that the porous sheet appears to be less effective at mid-enthalpies as compared to low and high enthalpies.

##### *Carbon Dioxide Shots*

An analysis similar to that performed for the nitrogen shots was also performed for each carbon dioxide shot. The resulting summary plot of  $Re_{tr}^*$  versus  $h_o$  is shown in Figure 17. Once again there is fairly good agreement between the present smooth surface results and those obtained in previous experiments by Adam, although there is much more scatter. This plot shows that the porous sheet was, in fact, detrimental at higher enthalpies, but was effective at lower enthalpies with a cross-over point at roughly 3.0 MJ/kg. The reason for this will be addressed in Section 4.1.7.

#### 4.1.6 Elimination of Other Causes for the Observed Effectiveness of the Porous Surface

As mentioned previously, the main objective of these experiments was to broadly test the computational prediction of Fedorov and Malmuth [12] by comparing the transition Reynolds

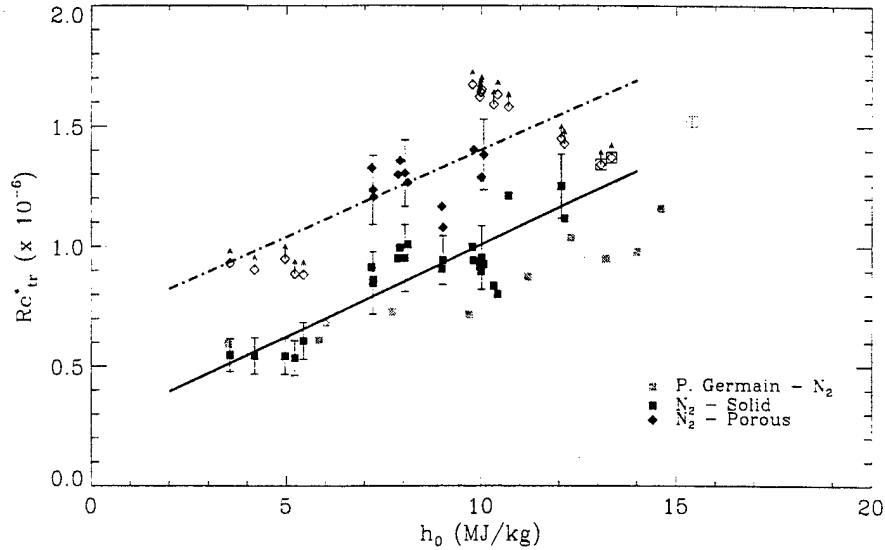


Figure 16: Plot of  $Re_{tr}^*$  versus  $h_0$  showing a summary of the nitrogen data. The dark data points are for the present experiments. The diamonds represent the  $Re_{tr}^*$  on the porous surface, while the squares represent the  $Re_{tr}^*$  on the smooth surface for the same shot. The grey squares represent the data obtained in previous experiments for a smooth surface at similar run conditions by Germain. The open symbols with upward facing arrows are used to indicate cases where the boundary layer was laminar over the entire length of the cone (they mark the last thermocouple location as being the transition location). The lines are linear curve fits to help guide the eye (dashed-dotted for porous, solid for smooth).

number on the smooth surface versus the porous surface for each shot. The previous sections partially validated the present results since transition on the smooth surface successfully reproduced the previous experiments by Germain [9] and Adam [10]. In order to completely confirm the effectiveness of the porous surface, however, it is necessary to eliminate other spurious effects. In particular, one must check the repeatability of the experiments, as well as verify that non-axisymmetry and angle-of-attack issues were not affecting the results.

#### *Repeatability*

Repeatability was tested by repeating selected experimental run conditions at various stages in the test program and noting that there was no observable effect on transition location. This was of particular importance since it confirmed that the accumulation of soot on the surface of the model had no effect on the experimental results. This observation is also an indication of the robustness of this boundary layer control scheme to small amounts of contamination.

#### *Angle-of-attack*

The effects of angle-of-attack on transition Reynolds number in hypersonic flow over a cone have been studied extensively. Previous experiments indicated that transition Reynolds number was a strong function of angle-of-attack near  $0^\circ$ . Stetson [36] performed experiments at

Mach 6 on a  $8^\circ$  half-angle cone and compared his results with other researchers including DiCristina ( $8^\circ$  cone,  $M=10$ ) [37], Holden ( $6^\circ$  cone,  $M=13.3$ ) [38], and Krogmann ( $5^\circ$  cone,  $M=5$ ) [39]. This last set of experiments by Krogmann most closely resembled the present experimental test conditions and, incidentally, demonstrated the most sensitivity of transition Reynolds number with angle-of-attack. In fact, an interpolation from his results revealed that transition Reynolds number varied by as much as 5% if the angle-of-attack varied by as little as  $0.1^\circ$ . For the present experiments, angle-of-attack was eliminated as a cause for the delayed transition by carefully aligning the model to within  $\pm 0.05^\circ$  of the tunnel axis. Furthermore, it was noted that the observed effect was to delay transition anywhere from 15% to 100% (or more since the cone was not long enough). This is significantly larger than the 5% variation attributable to angle-of-attack alone.

### Axisymmetry

Non-axisymmetry issues were addressed by rotating the model to the  $0^\circ$ ,  $90^\circ$  and  $180^\circ$  orientations and repeating the experiments. In particular, two run conditions were repeated and can be seen in Figure 16 as the three data points clustered at 5 MJ/kg and 8 MJ/kg. respectively. Clearly, there is excellent agreement and there appears to be no observable effects from lack of axial symmetry.

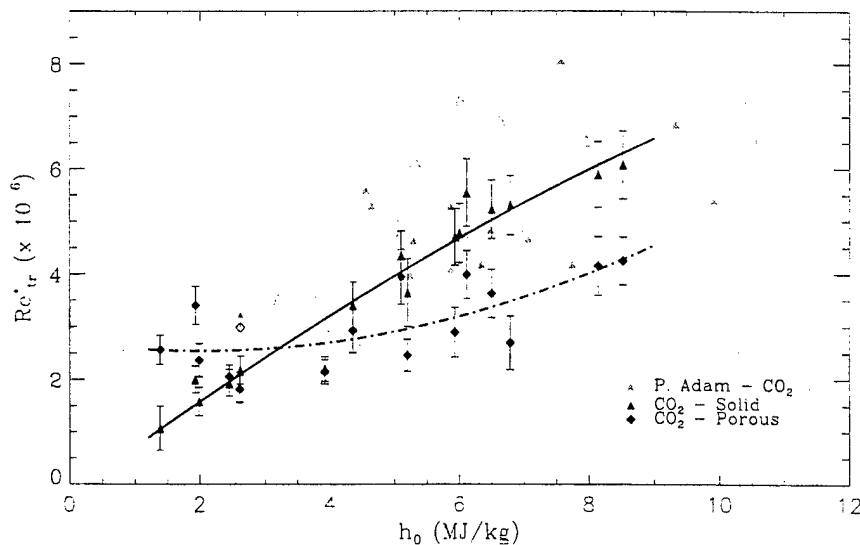


Figure 17: Plot of  $Re_{tr}^*$  versus  $h_0$  showing a summary of the carbon dioxide data. The dark data points are for the present experiments. The diamonds represent the  $Re_{tr}^*$  on the porous surface, while the triangles represent the  $Re_{tr}^*$  on the smooth surface for the same shot. The grey triangles represent the data obtained in previous experiments for a smooth surface at similar run conditions by Adam. The lines are 2<sup>nd</sup> order curve fits to help guide the eye (dashed-dotted for porous, solid for smooth).

#### 4.1.7 Effects of Surface Roughness

As mentioned previously, for the nitrogen experiments, the porous surface was effective over the whole enthalpy range tested; though it was more effective at low and high enthalpy conditions than at mid-enthalpy conditions. For the carbon dioxide shots, however, the porous surface was only effective at very low enthalpy conditions and was counter-productive at mid to high enthalpies. This interesting behavior suggested that another parameter was important in the carbon dioxide flows.

An explanation for the observed behavior lies in the expectation that the porous surface must be hydraulically smooth (*i.e.*, hole size must be sufficiently small in relation to the viscous length scale) in order for the proposed mechanism to effectively delay transition. If this were not the case, then the holes would act as distributed surface roughness and prematurely trip the boundary layer. A plot of  $Re_{tr,porous}^* - Re_{tr,smooth}^*$  versus  $Re_D^*$  (Reynolds number based on hole diameter) clearly shows that the delay in transition becomes much smaller as  $Re_D^*$  increases (see Figure 18). It should be noted that no such trend was observed when the results were plotted using the Reynolds number evaluated at the edge conditions ( $Re_D$ ) and it is, therefore, concluded that the reference Reynolds number is the proper Reynolds number to use in this analysis for these flows. The graph also shows that the mechanism becomes less effective at an  $Re_D^*$  of about 130 and actually prematurely trips the boundary layer at an  $Re_D^*$  greater than 300. For comparison, the Reynolds number evaluated at the viscous length scale was estimated at  $Re^+ \simeq 800$ . The most relevant experiment (to the present case) regarding distributed surface roughness effects was performed by Germain, who found that 0.1 mm salt crystals ( $Re_k^* = 220$ ) randomly distributed over the first 206 mm of the model tripped the boundary layer. No attempt was made to identify the 'critical' roughness Reynolds number below which the surface roughness had no effect on transition. For such a comparison, it is useful to recognize that the present results correspond reasonably well with experiments in incompressible flow by Feindt (as reported by Schlichting [40]) who examined the effect of distributed surface roughness (in the form of sand grains) on transition Reynolds number. Although the type of roughness was different from the current experiments (sand grains versus porous surface), Feindt also found that the surface roughness became important when  $Re_k$  (based on the sand grain height) was greater than 120. Similarly, Pfenninger [41] reported that surface roughness issues became important in laminar flow control experiments (suction through slots) when  $Re_s$  (based on slot width) was approximately greater than 100.

More recently, Reda [42] reviewed the effects of distributed surface roughness in hypersonic flows on nosetips, attachment lines and lifting entry vehicles. Reda concluded that there exists no universal value for critical  $Re_k$  (based on roughness height) for transition to turbulence and that this critical roughness Reynolds number was highly dependent on the particular flow field and roughness characteristics. Despite this observation, a number of different experiments indicate that the critical roughness Reynolds number is approximately 100 to 200. Reda's experiments [43] on nose tip transition in a ballistic range yielded values for the critical  $Re_k$  of 192. In other experiments, Bertin *et al.* [44] found  $Re_k = 110$  was the critical value at which roughness effects began to dominate in wind tunnel tests of a 0.0175 scale model of the Space Shuttle Orbiter at Mach 8 to 12. Furthermore, analysis by

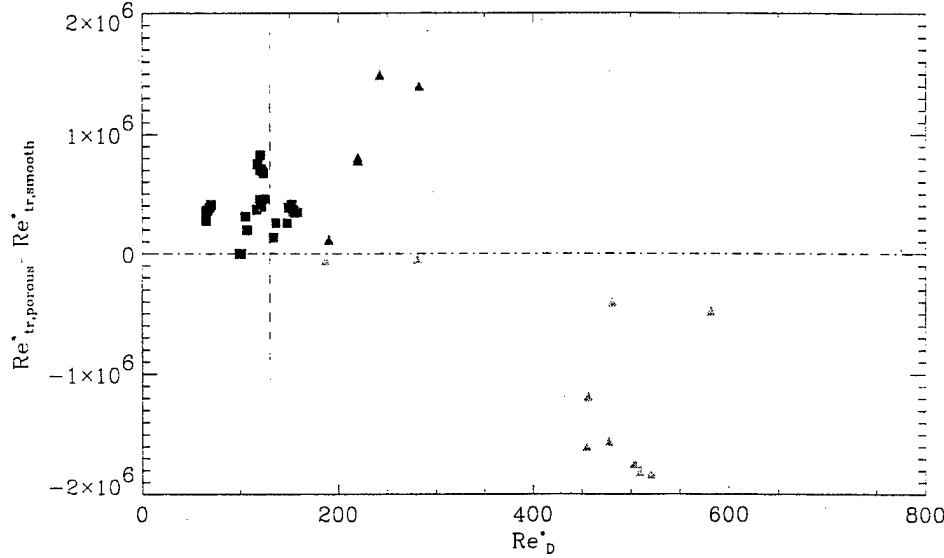


Figure 18: Plot showing the decreased effectiveness as  $Re_D^*$  increases beyond 130 (vertical line). The greyscale indicates the qualitative effectiveness of the porous surface. Black indicates laminar over the entire length of the cone on the porous side, medium grey indicates delayed transition was observed on the cone and light grey indicates premature transition. Squares and triangles correspond to  $N_2$  and  $CO_2$ , respectively.

Goodrich *et al.* [45] (as reported by Reda [42]) of transition data on the windward centerline of the Space Shuttle Orbiter during reentry for missions STS-1 to STS-5 suggest a critical  $Re_k$  of 120. It should be noted that in the above cases, the  $Re_k$  values were for surface bumps (as opposed to holes in the present work) and were calculated using the conditions in the boundary layer at the roughness height. This may or may not allow direct comparison with the  $Re_D^*$  used to analyze the present results, but it is clear that the critical  $Re_D^*$  is in the same range as previous experiments.

Finally, it should be noted that closer examination of Figure 18 also indicates that some parameter is still not fully accounted for since the effectiveness of the porous sheet does not decrease monotonically with increasing  $Re_D^*$ . Specifically, the porous sheet appeared to be more effective in the carbon dioxide shots at  $Re_D \simeq 200$  than the nitrogen shots at  $Re_D \simeq 130$ . It is not surprising that nitrogen and carbon dioxide behave slightly differently because the different chemistry involved affects the second mode amplification. In fact, this difference is probably the effect of enthalpy that had been noted earlier.

## 4.2 Resonantly Enhanced Shadowgraph

Further evidence of the effectiveness of the porous sheet is seen in Figure 19, which is a resonantly enhanced shadowgraph showing the boundary layer transitioning on the smooth surface while remaining laminar on the porous surface. This shadowgraph is from

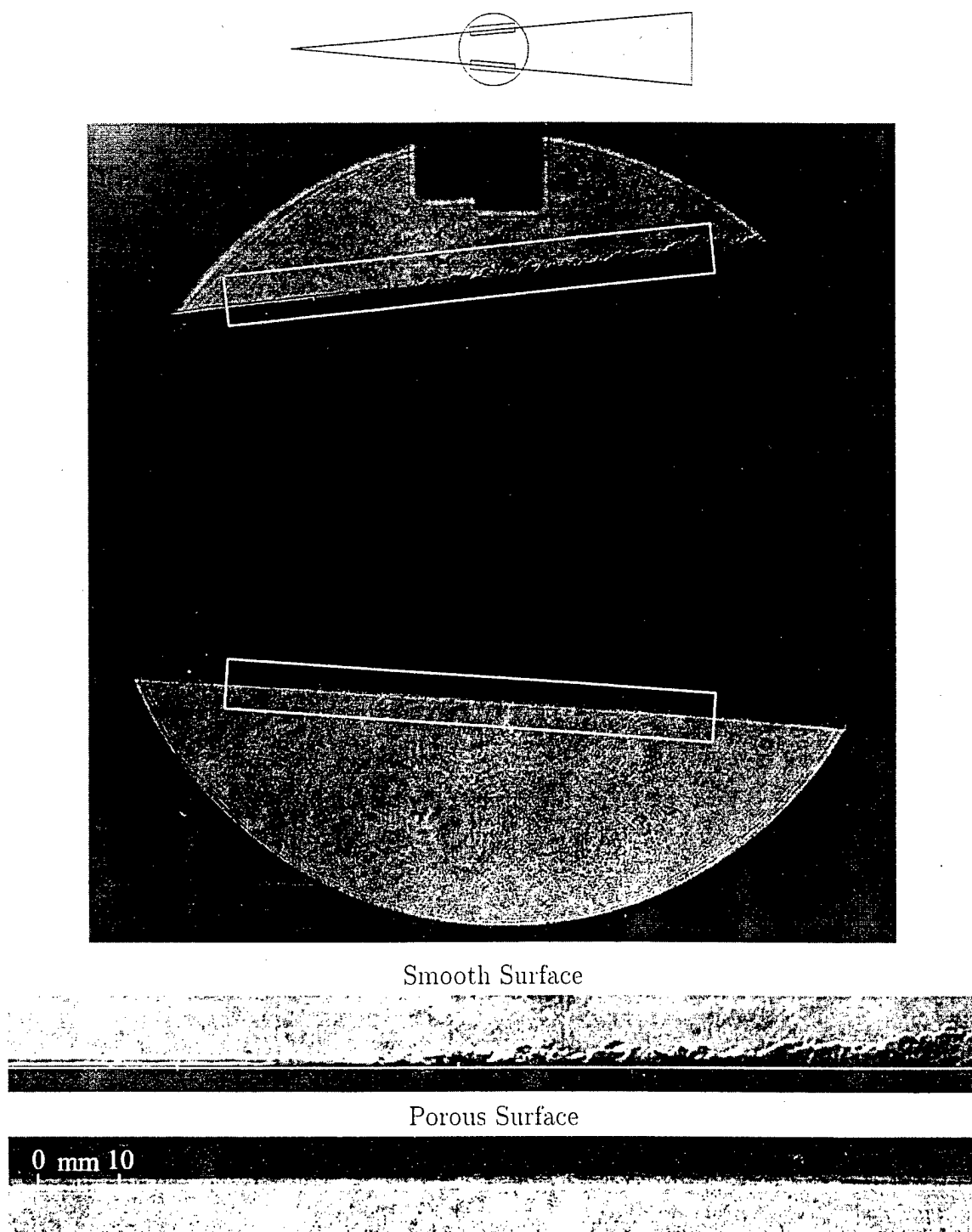


Figure 19: Resonantly enhanced shadowgraph for shot 2008 ( $P_o=48.2$  MPa,  $h_o=9.8$  MJ/kg) showing the boundary layer transitioning on the smooth surface (top) while remaining laminar on the porous surface (bottom). Flow is left to right and the schematic at the top indicates the window position relative to the model. The rectangular boxes in the main image indicate the location of the magnified images whose left and right edges are 495 mm and 615 mm from the cone tip, respectively (as measured along the surface of the cone). The white line on the magnified image of the smooth surface was digitally added to indicate the approximate surface of the model.



shot 2008 ( $P_o = 48.2$  MPa,  $h_o = 9.8$  MJ/kg) and was obtained by seeding the flow with sodium and tuning the frequency of the dye laser light source to the sodium D-line as described in Section 3.1.4. The transition location on the smooth surface identified by the analysis of the heat transfer data is approximately at the left edge of the magnified image of the smooth surface. These magnified images were also used to measure the laminar boundary layer thickness at the  $x = 495$  mm location. This boundary layer thickness was independently measured on both the smooth and porous surface, and both were found to be approximately  $1.2 \pm 0.15$  mm which is in agreement with Adam's computations [46]. It should be noted that these measurements are only approximate due to difficulties in accurately identifying the edge of the cone in the images and due to distortions from the optical integration across the test section and through the shear layer of the free-jet from the nozzle.

## 5 Conclusions

Extensive experiments testing a novel passive hypervelocity boundary layer transition control scheme have been carried out in the T5 Hypervelocity Shock Tunnel on a sharp  $5.06^\circ$  half-angle round cone with a smooth surface over half the cone and an ultrasonically absorptive porous surface over the other half. This boundary layer scheme was based on the results of a linear stability analysis whose details have been presented. In addition, the detailed flow physics responsible for the acoustic damping mechanism were examined. The experiments, performed in nitrogen and carbon dioxide, used heat transfer measurements to simultaneously determine the transition location on the smooth and porous surfaces for each shot. These new measurements for the smooth surface transition location compared very well with experimental results obtained by previous researchers in the same facility. The theoretical result that transition may be delayed by suitable wall porosity has been confirmed convincingly in nitrogen flows and the reversal of the phenomenon in carbon dioxide flows appears to be due to the chosen wall porosity scale being too coarse relative to the viscous length scale for high enthalpy run conditions. The results were tested for repeatability and were checked to insure that they were not induced by angle-of-attack or other effects. Finally, the effectiveness of the porous sheet was further evidenced by a resonantly enhanced shadowgraph that clearly showed transition occurring over the smooth surface but not on the porous surface.

## 6 Achievements

The project established experimentally that the theory of Fedorov and Malmuth, predicting that properly designed wall porosity can delay transition in hypersonic flow, is correct. The method can be used to achieve large reductions of heat loads on launch and reentry vehicles.

## 7 Personnel

Adam Rasheed, Graduate Research Assistant  
Bahram Valiferdowsi, Engineer (part time)  
Hans G. Hornung, Principal Investigator (part time)

## 8 Degrees

Adam Rasheed, Ph. D., 1999

## 9 Honors and Awards

Adam Rasheed:

California Institute of Technology C.L. Powell Fellowship (1996)  
Senate Medal for Outstanding Academic Achievement (1995)  
Pratt & Whitney Canada Award (1995)  
First Prize: Ontario Engineering Competition (1994) - Explanatory Communications  
David A. Golden Scholarship (1993 and 1994)  
Hewlett-Packard Award (1992)

Hans G. Hornung:

ICAS von Karman Award for International Cooperation in Aeronautics, 1989  
Scientific Member of the Board of the DLR, Germany, 1991  
Foreign member of the Royal Swedish Academy of Engineering Sciences, 1991  
Foreign Associate, National Academy of Engineering, 1997  
Ludwig Prandtl Ring, DGLR (German Society for Aeronautics and Astronautics), 1999

## 10 Publications resulting from the project

Rasheed, A., "Passive Hypervelocity Boundary Layer Control Using an Ultrasonically Absorptive Surface," Ph.D. Dissertation, California Institute of Technology, Pasadena, CA, 2001.

Rasheed, A., Hornung, H.G., Fedorov, A.V., and Malmuth, N.D., "Experiments on Passive Hypervelocity Boundary-Layer Control Using an Ultrasonically Absorptive Surface," *AIAA Journal*, Vol. 40, No. 3, March 2002.

Fedorov, A.V., Malmuth, N.D., Rasheed, A., and Hornung, H.G., "Stabilization of Hypersonic Boundary Layer by Porous Coatings," *AIAA Journal*, Vol. 39, No. 4, April 2001, pp. 605-610.

A. Rasheed, H.G. Hornung, A.V. Fedorov, N.D. Malmuth, "Experiments on passive hypervelocity boundary layer control using a porous surface", *AIAA Paper 2001-0274*, 2001.

A.V. Fedorov, N.D. Malmuth, A. Rasheed, H.G. Hornung, "Stabilization of Hypersonic Boundary Layer by Porous Coatings," *AIAA Paper 2001-0891*, 2001.

H. G. Hornung, K. Fujii, P. Germain and A. Rasheed, "On transition and transition control in hypervelocity flow", Plenary presentation in the 9th Asian Congress of Fluid Mechanics, Ishahan, Iran. May 2002, to be published in the Proceedings.

## References

- [1] L.M. Mack. Boundary-layer stability theory. In *Special Course on Stability and Transition of Laminar Flow*, AGARD Report Number 709, 1984.
- [2] A. Demetriades. An experiment on the stability of hypersonic laminar boundary layers. *Journal of Fluid Mechanics*, 7(3):385-396, 1960.
- [3] K.F. Stetson, E.R. Thompson, J.C. Donaldson, and L.G. Siler. Laminar boundary layer stability experiments on a cone at Mach 8. Part II: Blunt cone. *AIAA Paper 84-0006*, 1984. (22nd Aerospace Sciences Meeting and Exhibit, January 9-12, Reno, NV, USA).
- [4] J.M. Kendall. Wind tunnel experiments relating to supersonic and hypersonic boundary-layer transition. *AIAA Journal*, 13(3):290-299, 1975.
- [5] E. Reshotko. Boundary-layer stability and transition. *Annual Review of Fluid Mechanics*, 8:311-349, 1976.
- [6] M.R. Malik and E.C. Anderson. Real gas effects on hypersonic boundary-layer stability. *Physics of Fluids A*, 3(5):803-821, 1991.
- [7] G. Stuckert and H. Reed. Linear disturbances in hypersonic, chemically reacting shock layers. *AIAA Journal*, 32(7):1384-1393, 1994.
- [8] H.B. Johnson, T. Seipp, and G.V. Candler. Numerical study of hypersonic reacting boundary layer transition on cones. *Physics of Fluids*, 10(10):2676-2685, October 1998.
- [9] P. Germain and H.G. Hornung. Transition on a slender cone in hypervelocity flow. *Experiments in Fluids*, 22:183-190, 1997.

- [10] P. Adam and H.G. Hornung. Enthalpy effects on hypervelocity boundary layer transition: Ground test and flight data. *Journal of Spacecraft and Rockets*, 34(5):614-619, 1997.
- [11] A.V. Fedorov and N.D. Malmuth. Hypersonic flow stabilization by ultrasonically transparent wall. Technical Report SCNM96-1, Rockwell Science Center, 1996.
- [12] A.V. Fedorov, N.D. Malmuth, A. Rasheed, and H.G. Hornung. Stabilization of hypersonic boundary layer by porous coatings. AIAA Paper 2001-0891, 2001. (39th AIAA Aerospace Sciences Meeting and Exhibit, January 8-11, Reno, NV, USA).
- [13] H.G. Hornung. Experimental hypervelocity flow simulation, needs, achievements and limitations. In *Proceedings of the Pacific International Conference on Aerospace Sciences and Technology (PICAST)*, volume 1, pages 1-10, 1993. (National Cheng Kung University, Tainan, Taiwan, China).
- [14] N. Sudani and H.G. Hornung. Gasdynamical detectors of driver gas contamination in a high-enthalpy shock tunnel. *AIAA Journal*, 36(3):313-319, 1998.
- [15] N. Sudani, B. Valiferdowski, and H.G. Hornung. Test time increase by delaying driver gas contamination for reflected shock tunnels. *AIAA Journal*, 38(9):596-600, September 2000.
- [16] H.G. Hornung and J. Bélanger. Role and techniques of ground testing for simulation of flows up to orbital speed. AIAA Paper 90-1377, 1990. (16th Aerodynamic Ground Testing Conference, June 18-20, Seattle, WA, USA).
- [17] H.G. Hornung, B. Sturtevant, J. Bélanger, S. Sanderson, and M. Brouillette. Performance data of the new free-piston shock tunnel T5 at GALCIT. In *Proceedings of the 18th International Symposium on Shock Waves*, 1991. (Sendai, Japan).
- [18] H.G. Hornung. Performance data of the new free-piston shock tunnel T5 at GALCIT. AIAA Paper 92-3943, 1992. (17th Aerospace Ground Testing Conference, July 6-8, Nashville, TN, USA).
- [19] J.A. Lordi, R.E. Mates, and J.R. Moselle. Computer program for the numerical solution of nonequilibrium expansions of reacting gas mixtures. Technical Report NASA CR-472, National Aeronautics and Space Administration (NASA), 1966.
- [20] M. Rein. SURF: A program for calculating inviscid supersonic reacting flows in nozzles. Technical Report FM 89-1, GALCIT, California Institute of Technology, 1989.
- [21] B. Rousset. *Calibration and Study of the Contoured Nozzle of the T5 Free-Piston Hypervelocity Shock Tunnel*. Engineer's thesis, California Institute of Technology, 1995.
- [22] W.C. Reynolds. The element potential method of chemical equilibrium analysis: Implementation in the interactive program STANJAN. Technical report, Department of Mechanical Engineering, Stanford University, 1986.

- [23] M.K. McIntosh. A computer program for the numerical calculation of equilibrium and perfect gas conditions in shock tunnels. Technical Report CPD 169, Australian Defence Scientific Service, 1970.
- [24] P. Germain. *The Boundary Layer on a Sharp Cone in High-Enthalpy Flow*. PhD thesis. California Institute of Technology, 1994.
- [25] P. Lemieux. *The Instability of Shear Layers Produced by Curved Shocks*. PhD thesis. California Institute of Technology, 1999.
- [26] D. Bershader, S.G. Prakash, and G. Huhn. Improved flow visualization by use of resonant refractivity. *Progress in Astronautics and Aeronautics*, 53:595–609, 1977.
- [27] E.B. Cummings. *Laser-Induced Thermal Acoustics*. PhD thesis, California Institute of Technology, 1995.
- [28] D.J. Mee. Boundary layer transition measurements in hypervelocity flows in a shock tunnel. AIAA Paper 2001-0208, 2001. (39th AIAA Aerospace Sciences Meeting and Exhibit, January 8-11, Reno, NV, USA).
- [29] S.R. Sanderson. *Shock Wave Interaction in Hypervelocity Flow*. PhD thesis, California Institute of Technology, 1995.
- [30] J.P. Davis. *High-Enthalpy Shock/Boundary-Layer Interaction on a Double Wedge*. PhD thesis, California Institute of Technology, 1999.
- [31] ASTM. *Manual on the Use of Thermocouples in Temperature Measurement*, fourth edition, 1993.
- [32] D.L. Schultz and T.V. Jones. Heat transfer measurements in short duration hypersonic facilities. Technical Report AG-165, AGARD, 1973.
- [33] D. Kendall, W.P. Dixon, and E.H. Schulte. Semiconductor surface thermocouples for determining heat-transfer rates. *IEEE Transactions on Aerospace and Electronic Systems*, 3(4):596–602, July 1967.
- [34] W.H. Press, S.A. Teukolsky, W.T. Vetterling, and B.P. Flannery. *Numerical Recipes in FORTRAN: The Art of Scientific Computing*. Cambridge University Press, 1992.
- [35] B. Sundqvist. Thermal diffusivity and thermal conductivity of chromel, alumel, and constantin in the range 100-450 K. *Journal of Applied Physics*, 72(2):539–545, 1972.
- [36] K.F. Stetson. Mach 6 experiments of transition on a cone at angle of attack. *Journal of Spacecraft and Rockets*, 19(5):397–403, 1982.
- [37] V. DiCristina. Three dimensional laminar boundary transition on a sharp 8 deg cone at mach 10. *AIAA Journal*, 8(5):852–856, 1970.

- [38] M. Holden. Studies of the effects of transitional and turbulent boundary layers on the aerodynamic performance of hypersonic re-entry vehicles in high reynolds number flows. Technical Report AFOSR-TR-79-0125, Airforce Office of Scientific Research, 1978.
- [39] P. Krogmann. Experimentelle Untersuchungen über Strömung an Kegeln. *Z. Flugwiss. Weltraumforsch.*, 2:108–115, 1977.
- [40] H. Schlichting. *Boundary Layer Theory*. McGraw-Hill Company, 1987.
- [41] W. Pfenninger. Laminar flow control. In *Special Course on Concepts for Drag Reduction*, AGARD Report Number 654, 1977.
- [42] D.C. Reda. Roughness-dominated transition on nosetips, attachment lines and lifting-entry vehicles. AIAA Paper 2001-0205, 2001. (39th AIAA Aerospace Sciences Meeting and Exhibit, January 8-11, Reno, NV, USA).
- [43] D.C. Reda. Correlation of nosetip boundary-layer transition data measured in ballistics-range experiments. *AIAA Journal*, 19(3):329–339, 1981.
- [44] J.J. Bertin, T.E. Hayden, and W.D. Goodrich. Shuttle boundary-layer transition due to distributed surface roughness and surface cooling. *Journal of Spacecraft and Rockets*, 19(5):389–396, 1982.
- [45] W.D. Goodrich, S.M. Derry, and J.J. Bertin. Shuttle orbiter boundary layer transition at flight and wind tunnel conditions. In *Shuttle Performance: Lessons Learned*, March 1983. (NASA Conference Publication 2283, Part 2).
- [46] P. Adam. *Enthalpy Effects on Hypervelocity Boundary Layers*. PhD thesis, California Institute of Technology, 1997.